

Deterministic and Probabilistic Neural Surrogates of Global Hybrid-Vlasov Simulations

Daniel Holmberg^{1,3}, Ivan Zaitsev², Markku Alho², Ioanna Bouri¹, Fanni Franssila¹, Haewon Jeong³, Minna Palmroth^{2,4}, Teemu Roos¹

¹Department of Computer Science, University of Helsinki

²Department of Physics, University of Helsinki

³Department of Electrical and Computer Engineering, University of California, Santa Barbara

⁴Space and Earth Observation Centre, Finnish Meteorological Institute

Key Points:

- Graph neural networks can be used to emulate global hybrid-Vlasov plasma simulations orders of magnitude faster than the physics model.
- Probabilistic graph-based ensemble forecasting enables uncertainty-aware prediction of future plasma states.
- The machine learning models reproduce physical magnetospheric structures such as the bow shock and magnetotail in high detail.

Abstract

Hybrid-Vlasov simulations resolve ion-kinetic effects for modeling the solar wind-magnetosphere interaction, but even 5D (2D + 3V) simulations are computationally expensive. We show that graph-based machine learning emulators can learn the spatiotemporal evolution of electromagnetic fields and lower order moments of ion velocity distribution in the near-Earth space environment from four 5D Vlasiator runs performed with identical steady solar wind conditions. The initial ion number density is systematically varied, while the grid spacing is held constant, to scan the ratio of the characteristic ion skin depth to the numerical grid size. Using a graph neural network architecture operating on the 2D spatial simulation grid comprising 670k cells, we demonstrate that both a deterministic forecasting model (Graph-FM) and a probabilistic ensemble forecasting model (Graph-EFM) based on a latent variable formulation are capable of producing accurate predictions of future plasma states. A divergence penalty is incorporated during training to encourage divergence-freeness in the magnetic fields and improve physical consistency. For the probabilistic model, a continuous ranked probability score objective is added to improve the calibration of the ensemble forecasts. When trained, the emulators achieve more than two orders of magnitude speedup in generating the next time step relative to the original simulation on a single GPU compared to 100 CPUs for the Vlasiator runs, while closely matching physical magnetospheric response of the different runs. These results demonstrate that machine learning offers a way to make hybrid-Vlasov simulation tractable for real-time use while providing forecast uncertainty.

Plain Language Summary

Space weather, electromagnetic disturbances in near-Earth space driven by the solar wind, can disrupt satellites, communications, and power grids. The most accurate scientific tools for modeling and understanding the processes controlling space weather are large-scale ion-kinetic plasma simulations. These are too computationally expensive to run in real-time or to generate the many ensemble members needed to estimate forecast uncertainty. In this study, we show that machine learning can make these simulations much faster. We train data-driven models based on numerical space simulations so that they can learn how conditions in Earth's space environment evolve over time. Once trained, these models can produce forecasts more than one hundred times faster than the original simulator, while still faithfully capturing the physical features of the system. These results show that machine learning can pave the way for effective utilization of computational resources while performing global ion-kinetic simulations, including the ability to generate fast ensembles that can be used to quantify the uncertainty in future plasma states.

1 Introduction

Space weather encompasses the solar wind-driven electromagnetic variability of near-Earth space and the internal dynamics of Earth's magnetosphere, which leads to the induction of geomagnetic field perturbations down to the Earth's surface (Baker, 1998). Geomagnetically induced currents can disrupt power networks (Bolduc, 2002; Dimmock et al., 2019), satellites experience enhanced drag and operational anomalies (Gubby & Evans, 2002; Zhang et al., 2022), and radio communication systems can fail during disturbed conditions (Baker et al., 2004). Accurate and reliable forecasting is therefore essential for mitigating the societal and technological risks associated with extreme space-weather events.

Near-Earth space-weather forecasting predominantly relies on global magnetohydrodynamic (MHD) models such as GUMICS-4 (Janhunen et al., 2012) or BATS-R-US (Glocer et al., 2013), driven by real-time solar wind measurements from Lagrange 1 (L1) monitors like ACE (Stone et al., 1998). While efficient, MHD models approximate plasma

as a fluid and thus omit ion-kinetic processes that play a fundamental role in near-Earth space. Hybrid-Vlasov simulations capture these kinetic dynamics by evolving the ion velocity distribution function (VDF). Vlasiator (Von Alfthan et al., 2014; Palmroth et al., 2018, 2025) is a leading example, enabling detailed investigations of magnetospheric phenomena such as magnetotail reconnection (Palmroth et al., 2023), transmission of fore-shock waves through the bow shock (Turc et al., 2023), or magnetosheath jets (Suni et al., 2025). However, their computational cost renders them unsuitable for real-time use.

In an attempt to speed up numerical simulation, neural surrogates have advanced rapidly in recent years, with approaches based on neural operators (Li et al., 2020), convolutional neural networks (Kochkov et al., 2021), or graph neural networks (GNNs) (Pfaff et al., 2021; Lino et al., 2022). Such approaches have been applied also for plasmas across a range of fidelities and geometries. Neural operators have been proposed as surrogates for MHD simulations (Gopakumar et al., 2024; Carey et al., 2025). GNNs have been applied to learn the dynamics of a one-dimensional plasma sheet model (Carvalho et al., 2024), and to emulate particle-in-cell simulations (Mlinarević et al., 2025). GNNs have further been used to approximate elliptic subproblems such as the Poisson equation on unstructured grids for Hall thruster modeling (Vigot et al., 2025). In terms of space weather, echo state networks have been used to emulate the auroral current system (Kataoka et al., 2024), GNNs have been developed to forecast total electron content in the ionosphere (Kelebek et al., 2025), and the spherical Fourier neural operator has been adopted to predict the radial velocity of the solar wind in the heliosphere (Mansouri et al., 2025).

A limitation of these plasma surrogates is their reliance on deterministic single-point forecasts. Addressing this, in particular, would also be beneficial for space weather forecasting, where ensemble approaches have been advocated to quantify forecast uncertainty (Murray, 2018). Existing demonstrations include using an ensemble of four independent models to predict major solar flares, which yielded better skill than any single model (Guerra et al., 2015); ensemble modeling of coronal mass ejections to quantify uncertainty in their arrival times (Mays et al., 2015); perturbing solar wind conditions upstream of the bow shock based on L1 observations and propagating these through the Space Weather Modeling Framework (Morley et al., 2018); and applying machine-learning post-processing to generate probabilistic forecasts (Camporeale et al., 2019). Despite these efforts, uncertainty-aware forecasting remains uncommon in space weather, largely because physics-based modeling makes ensemble generation computationally expensive.

To help tackle these challenges, we take inspiration from recent breakthroughs in machine learning for atmospheric weather forecasting (Ben Bouallegue et al., 2024), where both deterministic (Keisler, 2022; Bi et al., 2023; Lam et al., 2023) and probabilistic models (S. Lang et al., 2024; Oskarsson et al., 2024; Price et al., 2025; Alet et al., 2025), could offer new ways to achieve high-fidelity, data-driven models for space weather. In particular, we adapt GNN architectures (Keisler, 2022; Oskarsson et al., 2024) to emulate plasma dynamics in the noon–midnight meridional plane of the Earth’s magnetosphere. We compile a high-resolution dataset comprising four global Vlasiator simulations, each driven by a distinct solar wind, and train the GNN emulators on the electromagnetic fields and the plasma moments of the dataset. The resulting emulators can then produce forecasts of magnetospheric plasma evolution more than two orders of magnitude faster on a single GPU than the original simulation running on 100 CPUs, incorporating learned kinetic effects from the underlying dataset. Furthermore, the framework supports both deterministic forecasting and probabilistic ensemble generation through a latent-variable formulation that yields forecast uncertainty. The dataset (Zaitsev et al., 2025) and code (Holmberg, 2025) are released openly to facilitate detailed machine learning studies of kinetic-scale magnetospheric dynamics, and the adoption of probabilistic neural surrogates in space weather research.

2 Hybrid-Vlasov Dataset

The data for this study were generated using Vlasiator, which performs global simulations of the solar wind's interaction with the Earth's magnetosphere in the hybrid-Vlasov formalism. Ions are treated as a VDF, f , that depends on position \mathbf{x} , velocity \mathbf{v} , and time t . Its evolution is dictated by the Vlasov equation, which describes how f changes due to the electric field \mathbf{E} and magnetic field \mathbf{B} :

$$\frac{\partial f}{\partial t} + \mathbf{v} \cdot \frac{\partial f}{\partial \mathbf{x}} + (\mathbf{E} + \mathbf{v} \times \mathbf{B}) \cdot \frac{\partial f}{\partial \mathbf{v}} = 0. \quad (1)$$

Electrons are modeled as a massless, charge-neutralizing fluid where the number density n is equal for both ions and electrons ($n_i \simeq n_e \simeq n$). The electromagnetic fields are evaluated by solving the Maxwell-Darwin system:

$$\nabla \times \mathbf{E} = -\partial_t \mathbf{B}, \quad \nabla \times \mathbf{B} = \mu_0 \mathbf{J}, \quad \nabla \cdot \mathbf{B} = 0. \quad (2)$$

This system is closed by relating the fields to the moments of the ion distribution function through a generalized Ohm's law that includes the Hall term, which involves the current density \mathbf{J} and the elementary charge e :

$$\mathbf{E} + \mathbf{v} \times \mathbf{B} = \frac{\mathbf{J} \times \mathbf{B}}{ne}. \quad (3)$$

All simulations are performed in 2D + 3V (two spatial and three velocity dimensions) on the noon–midnight meridional plane in Geocentric Solar Ecliptic (GSE) coordinate system. The spatial grid is static, Cartesian and uniformly spaced with the resolution of 600 km. The spatial domain spans $x \in [-60, 30] R_E$ and $z \in [-30, 30] R_E$. The velocity space is also represented by a Cartesian grid, with a uniform resolution of 52 km/s. The temporal cadence of the simulations is $dt = 0.035$ s. The cadence of the reduced output files is $\Delta t = 1$ s. The inner boundary at $r = 3.7 R_E$ is modeled as a perfect conductor, while the dayside inflow boundary injects a Maxwellian solar wind. The outflow boundaries at $\pm z$ and $-x$ employ copy conditions, while the y direction is treated as a periodic dimension with a single layer of cells.

The simulations are carried out in the $(x-z)$ plane at $y = 0$. This plane lies along the Sun–Earth line and includes the geomagnetic dipole axis, and has been shown to capture key features such as the collisionless bow shock, ion foreshock, and magnetosheath (Von Alfthan et al., 2014), as well as magnetic reconnection at the dayside magnetopause (Hoilijoki et al., 2017) and in the magnetotail (Palmroth et al., 2017). Restricting the simulations to two spatial dimensions implies an out-of-plane symmetry with no gradients in that direction, i.e. $\partial/\partial y = 0$. As a result, large-scale transport of magnetic flux around the magnetosphere via the dawn–dusk flanks is suppressed, and in configurations with southward interplanetary magnetic field the solar-wind flux must reconnect directly on the dayside. While this removes certain global transport pathways, the 2D + 3V approximation remains physically meaningful for many magnetospheric processes.

To probe the parameter space, we vary the solar wind ion density while keeping the velocity, temperature, and interplanetary magnetic field fixed. As shown in Table 1, increasing the density systematically raises the Alfvén Mach number M_A , moving the system from moderately super-Alfvénic (Run 1, $M_A = 4.9$) to strongly super-Alfvénic flow (Run 4, $M_A = 9.8$). Because the bow shock standoff distance and the overall magnetospheric morphology depend sensitively on M_A , this controlled sweep provides a dataset spanning a range of relevant physical regimes. Varying the density changes the ion inertial length and therefore the ratio between kinetic scales and the fixed grid spacing.

Table 2 summarizes all physical variables included in the Vlasiator dataset, listing their notation, units, and the residual standard deviation of each variable for each

Table 1. Solar wind parameters at the dayside boundary, and time step information for each simulation run.

Label	ρ (cm $^{-3}$)	\mathbf{v} (km/s)	\mathbf{B} (nT)	T (MK)	M_A	Δt (s)	t_{tot} (s)
Run 1	0.5	(-750, 0, 0)	(0, 0, -5)	0.5	4.9	1.0	800
Run 2	1.0	(-750, 0, 0)	(0, 0, -5)	0.5	6.9	1.0	800
Run 3	1.5	(-750, 0, 0)	(0, 0, -5)	0.5	8.4	1.0	800
Run 4	2.0	(-750, 0, 0)	(0, 0, -5)	0.5	9.8	1.0	800

of the four simulation runs. These residuals are computed after normalization, and provide a measure of the intrinsic variability of each variable. We use these residual standard deviations as weights in the loss function when training our machine learning models as a way to normalize by the magnitude of the dynamics when predicting the evolution of the system. The plasma variables correspond to standard moments of the ion velocity distribution function: the zeroth moment gives the ion number density ρ , defined as the integral of the ion distribution function over velocity space; the first moment yields the bulk flow velocity \mathbf{v} , representing the mean direction and speed of ion motion; and the second central moments appear as the scalar pressure P and derived temperature T , which measure the thermal energy density and the intensity of random ion motions about the mean flow. In addition to the variables a few static fields comprising the coordinates (x, z) and the radial distance r from the origin are included as extra positional information. The data is stored in Zarr format (Miles et al., 2024) in an open repository (Zaitsev et al., 2025).

Table 2. Summary of all variables in the Vlasiator dataset, including notation, unit and residual standard deviation for each simulation run.

Variable	Label	Unit	Run 1	Run 2	Run 3	Run 4
			σ_{Res}	σ_{Res}	σ_{Res}	σ_{Res}
Magnetic field x -component	B_x	nT	0.116	0.105	0.101	0.096
Magnetic field y -component	B_y	nT	0.124	0.120	0.109	0.121
Magnetic field z -component	B_z	nT	0.132	0.132	0.144	0.146
Electric field x -component	E_x	mV/m	0.143	0.103	0.088	0.093
Electric field y -component	E_y	mV/m	0.310	0.209	0.189	0.216
Electric field z -component	E_z	mV/m	0.192	0.153	0.142	0.168
Velocity field x -component	v_x	km/s	9.748	6.971	5.488	5.385
Velocity field y -component	v_y	km/s	10.08	7.144	5.697	6.096
Velocity field z -component	v_z	km/s	10.97	8.044	6.410	6.100
Particle number density	ρ	1/cm 3	0.007	0.010	0.015	0.016
Plasma pressure	P	nPa	0.003	0.004	0.005	0.005
Plasma temperature	T	MK	1.214	0.812	0.720	0.631

3 Methods

3.1 Problem Formulation

We formulate the problem of space weather forecasting as mapping a set of initial magnetospheric states to a sequence of future states as shown in Figure 1. The input consists of two consecutive states, $X^{-1:0} = (X^{-1}, X^0)$, to capture first-order dynamics (Lam et al., 2023), with the goal of predicting the future trajectory $X^{1:T} = (X^1, \dots, X^T)$,

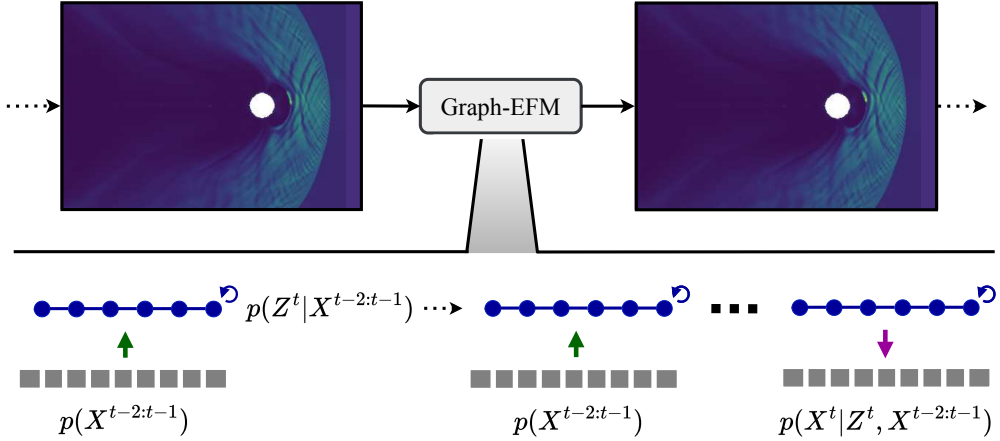


Figure 1. Schematic overview of the Graph-EFM forecasting framework. The input simulation state (particle number density depicted here) is given to the model, which consists of two components: a latent map that converts the two most recent states into a distribution over a low-dimensional latent variable, and an encode–process–decode process that maps the input history and a sampled latent value to the next predicted state. The Graph-FM model used for comparison is only composed of the deterministic mapping from the two previous simulation steps to the following one. Finally, the predicted state can be concatenated to the previous step and given back as input, enabling multi-step rollouts.

where T denotes the forecast horizon. Each magnetospheric state $X^t \in \mathbb{R}^{N \times F}$ is a high-dimensional tensor representing F physical variables present in the hybrid-Vlasov simulation across N grid locations in near-Earth space. Deterministic models tackle the problem by producing a single point, typically mean, estimate of the trajectory $X^{1:T}$, while probabilistic approaches aim to model the full conditional distribution $p(X^{1:T} | X^{-1:0})$.

3.2 Graph-Based Neural Forecasting

Using machine learning, the deterministic forecasting problem can be solved with an autoregressive model applied iteratively to produce a forecast. In the probabilistic case, we sample from the model’s output distribution and repeat the process to generate an ensemble of trajectories. For both cases, we use a GNN based on an *encode-process-decode* architecture (Sanchez-Gonzalez et al., 2020). In the encoding stage, the physical variables defined on the high-resolution simulation grid are projected onto a coarser mesh, where each mesh node receives information from its corresponding grid neighborhood. During the processing stage, several GNN message-passing layers operate on this mesh graph, allowing information to propagate laterally across mesh nodes and expanding each node’s receptive field. In the decoding stage, the updated mesh features are mapped back to the original grid via directed mesh-to-grid edges to produce the next predicted state. The GNN outputs a *residual update* to the most recent input state, making it an easier learning task compared to predicting the next state directly.

We construct our mesh graph \mathcal{G}_M for our forecasting models by recursively down-sampling the simulation grid. This produces a quadrilateral mesh structure (Oskarsson et al., 2024) composed of one mesh layer coarser than the simulation domain (Keisler, 2022). Information flows between representations via three edge sets: grid-to-mesh, with edges directed from grid nodes to mesh nodes; mesh-to-mesh, whose edges are bidirec-

tional and support lateral message passing within the mesh; and mesh-to-grid, with edges directed from mesh nodes back to grid nodes.

To ensure accurate handling of open boundary conditions at the solar wind inflow region on the Earth’s dayside one could apply a boundary forcing at the domain edge by specifying which grid nodes are to be replaced with ground truth boundary data after each prediction (Holmberg et al., 2025). However, since the simulations in this work are driven by four distinct but constant solar wind conditions, this is not strictly necessary, as the model is given all the information necessary to learn the corresponding steady inflow for a given initial state without explicit boundary forcing. For experiments involving time-varying boundary conditions, this effect should be modeled explicitly. In an operational context, such information could be incorporated through conditioning on upstream L1 solar wind observations (Glocer et al., 2013; Honkonen et al., 2022) or on the inner boundary of a heliospheric host model (Maharana et al., 2024).

3.3 Deterministic Model

We use the deterministic graph-based forecasting model *Graph-FM* (Oskarsson et al., 2024) to generate point estimate forecasts through the autoregressive mapping $\hat{X}^t = f(X^{t-2:t-1})$. GNN message passing is performed to encode information from the grid to the coarser mesh, then a number of GNN message passing processing steps takes place on this coarser mesh, and a final decoding using GNNs is performed to map back to the next simulation grid state. All upward updates are facilitated by *propagation networks* (Oskarsson et al., 2024), while the remaining updates use *interaction networks* (Battaglia et al., 2016), with all layers mapping to a latent dimensionality d_z . This design leverages the inductive bias of interaction networks to retain information, while propagation networks are more effective at forwarding new information through the graph. We train the deterministic models by minimizing a weighted mean square error (MSE) loss.

3.4 Probabilistic Model

For probabilistic forecasting we employ the graph-based ensemble forecasting model, *Graph-EFM* (Oskarsson et al., 2024). To model the distribution $p(X^t|X^{t-2:t-1})$ for a single time step, Graph-EFM uses a latent random variable Z^t . This variable acts as a low-dimensional representation of the stochastic elements of the system that are not captured by the input states. By conditioning the prediction on this latent variable, the model can efficiently sample different, spatially coherent outcomes. The relationship is defined by the integral:

$$p(X^t|X^{t-2:t-1}) = \int p(X^t|Z^t, X^{t-2:t-1})p(Z^t|X^{t-2:t-1})dZ^t \quad (4)$$

where the term $p(Z^t|X^{t-2:t-1})$ is the latent map and the term $p(X^t|Z^t, X^{t-2:t-1})$ is the predictor. The latent map is a probabilistic mapping that takes the previous two states as input and produces the parameters for a distribution over the latent variable Z^t . Specifically, Graph-EFM uses GNNs to map the inputs to the mean of an isotropic Gaussian distribution, effectively encoding the state-dependent uncertainty into the latent space. The variance is kept fixed. This latent distribution is defined over the nodes \mathcal{V}_M in the coarse mesh graph, as follows:

$$p(Z^t|X^{t-2:t-1}) = \prod_{v \in \mathcal{V}_M} \mathcal{N}(Z_v^t | \mu_Z(X^{t-2:t-1})_v, I), \quad (5)$$

ensuring that the stochasticity is introduced at a low-dimensional, spatially-aware level. The predictor is a deterministic mapping that takes a specific sample of the latent variable Z^t , along with the previous states, to produce the next state \hat{X}^t . A sampled value of Z^t is injected at the top level of the graph hierarchy and its influence propagates down through the levels to produce a full, high-resolution, and spatially coherent forecast. The

predictor is a deterministic mapping, g , that produces the next state \hat{X}^t by adding a predicted residual update, \tilde{g} , to the previous state X^{t-1} :

$$\hat{X}^t = g(Z^t, X^{t-2:t-1}) = X^{t-1} + \tilde{g}(Z^t, X^{t-2:t-1}). \quad (6)$$

By first sampling a Z^t from the latent map and then passing it through the predictor, the model generates one possible future state. Repeating this process creates an arbitrarily large ensemble of forecasts. Drawing from the structure of a conditional Variational Autoencoder (VAE) (Kingma & Welling, 2014; Sohn et al., 2015), we train the Graph-EFM by optimizing a variational objective equivalent to the negative Evidence Lower Bound (ELBO), which combines a Kullback-Leibler (KL) divergence regularizer with a reconstruction loss. Subsequently, we fine-tune the model by adding a Continuous Ranked Probability Score (CRPS) loss (Gneiting & Raftery, 2007; Rasp & Lerch, 2018; Pacchiardi et al., 2024) to the objective, for calibration.

3.5 Model Details

The 1006×671 (x, z) data grid excludes 5124 inner boundary nodes close to the Earth. The mesh used by the models is constructed by placing each mesh node at the center of a 5×5 square of finer simulation grid cells. The full statistics of this graph including graph-to-mesh and mesh-to-graph connections are shown in Table 3. For each node, an MLP encodes static features in Table 2, concatenated with previous states. For a complete explanation on update rules in the GNNs see (Oskarsson et al., 2024). All MLPs use one hidden layer with Swish activation and layer normalization.

Table 3. Number of nodes and edges in the mesh graph.

Graph	Nodes	Edges
\mathcal{G}_M	15496	122344
\mathcal{G}_{G2M}	-	669902
\mathcal{G}_{M2G}	-	2009706
Grid	669902	-

Some modifications to the model were necessary to enable training on our substantially larger grid of 669,902 nodes, compared to the grid sizes used in Oskarsson et al. (2024) with 29,040 grid nodes for global weather and 63,784 for limited-area weather. First, we construct the multi-resolution meshes using a coarser 5×5 downsampling ratio instead of 3×3 , reducing the number of nodes in the mesh graph. Second, in the mesh-to-grid mapping stage, each grid node is connected to its three nearest mesh nodes rather than four to reduce the size of the mapping with the largest number of edges in the architecture, constituting a main memory bottleneck, while still providing an interpolation stencil spanning the plane. Third, we introduce an additional MLP prior to the mesh-to-grid projection, defining an intermediate dimension d_{M2G} as this directly affects the largest matrix multiplication in the model. These design choices allow us to increase the latent dimension while still being able to fit the model in GPU memory, and empirically they also do not seem to produce visual artifacts. Finally, we apply gradient checkpointing (Chen et al., 2016) across rollout steps, ensuring that GPU memory usage remains effectively constant when increasing rollout length during training, while compute time scales approximately linearly with the number of steps. The code is implemented in PyTorch Lightning (v2.4.0) (Falcon et al., 2024) and made openly available (Holmberg, 2025).

3.6 Deterministic Objective

We train the deterministic models by minimizing a weighted MSE:

$$\mathcal{L}_{\text{MSE}} = \frac{1}{TN} \sum_{t=1}^T \sum_{n=1}^N \sum_{i=1}^{d_x} \frac{\lambda_i}{d_x} \left(\hat{X}_{n,i}^t - X_{n,i}^t \right)^2. \quad (7)$$

The loss weight λ_i is the inverse variance of the time differences for variable i , which normalizes the contribution of variables with different dynamic ranges (Keisler, 2022).

To encourage physical consistency, we augment the deterministic training loss with a divergence penalty enforcing $\nabla \cdot \mathbf{B} = 0$. The divergence loss is defined as

$$\mathcal{L}_{\text{Div}} = \frac{1}{TN} \sum_{t=1}^T \sum_{n=1}^N \left(\frac{\partial \hat{B}_x^t}{\partial x} + \frac{\partial \hat{B}_z^t}{\partial z} \right)_n^2, \quad (8)$$

where the divergence $\nabla \cdot \hat{\mathbf{B}} = \partial_x \hat{B}_x + \partial_z \hat{B}_z$ is computed over the interior grid points. Analogous to how divergence may accumulate over time in MHD simulations (Janhunen et al., 2012) and is removed using projection methods (Brackbill & Barnes, 1980), we optimize the soft constraint over multiple rollout steps T to prevent long-term buildup of divergence. The spatial derivatives are discretized using second-order central differences,

$$\left. \frac{\partial \hat{B}_x}{\partial x} \right|_{i,j} \approx \frac{\hat{B}_x(x_{i+1}, z_j) - \hat{B}_x(x_{i-1}, z_j)}{2 \Delta x}, \quad (9)$$

$$\left. \frac{\partial \hat{B}_z}{\partial z} \right|_{i,j} \approx \frac{\hat{B}_z(x_i, z_{j+1}) - \hat{B}_z(x_i, z_{j-1})}{2 \Delta z}, \quad (10)$$

yielding second-order accurate estimates on the interior stencil. The final deterministic training objective becomes

$$\mathcal{L} = \mathcal{L}_{\text{MSE}} + \lambda_{\text{Div}} \mathcal{L}_{\text{Div}}, \quad (11)$$

where λ_{Div} controls the strength of the divergence penalty.

3.7 Probabilistic Objective

The probabilistic model's single-step prediction has a structure analogous to a conditional VAE, and it is trained by optimizing a variational objective derived from the ELBO:

$$\begin{aligned} \tilde{\mathcal{L}}_{\text{Var}}(X^{t-2:t-1}, X^t) &= \sum_{t=1}^T \lambda_{\text{KL}} D_{\text{KL}}(q(Z^t | X^{t-2:t-1}, X^t) || p(Z^t | X^{t-2:t-1})) \\ &\quad - \mathbb{E}_{q(Z^t | X^{t-2:t-1}, X^t)} \left[\sum_{n=1}^N \sum_{i=1}^{d_x} \log \mathcal{N}(X_{v,i}^t | g(Z^t, X^{t-2:t-1})_{v,i}, \sigma_{v,i}^2) \right]. \end{aligned} \quad (12)$$

Here, the variational distribution $q(Z^t | X^{t-2:t-1}, X^t)$ provides a learned approximation to the intractable true posterior $p(Z^t | X^{t-2:t-1}, X^t)$ over the latent variables Z^t . This distribution is parameterized in a similar way as the latent map used for forecasting: a set of GNN layers encodes the inputs and produces the mean and variance of a Gaussian distribution over Z^t . Unlike the prior $p(Z^t | X^{t-2:t-1})$, the variational approximation q is posterior-facing, i.e. it also conditions on the target state X^t in order to match the true posterior as closely as possible, consistent with standard variational inference. This objective consists of two terms. The first is the KL divergence, which acts as a regularizer, encouraging the approximate posterior q to remain close to the prior p . The second term is the expected negative log-likelihood, or reconstruction loss, which trains the

predictor g to accurately reconstruct the true state X^t from a latent sample Z^t . The hyperparameter λ_{KL} balances these terms to prevent the model from collapsing to a deterministic prediction. Because both distributions are Gaussian, the KL divergence has a closed-form solution. The predictive variance $\sigma_{v,i}^2$ is produced by the decoder network.

As in the deterministic setting, we roll out the forecasts over multiple time steps to promote long-term stability. The multi-step objective is defined as:

$$\mathcal{L}_{\text{Var}} = \sum_{t=1}^T \tilde{\mathcal{L}}_{\text{Var}} \left(\hat{X}_{t-2:t-1}, X_t \right) \quad (13)$$

where \hat{X}_t denotes an initial state from the dataset for $t < 1$, and for $t \geq 1$ is obtained by sampling from the variational approximation of Z^t .

The model is further fine-tuned using the CRPS loss, which is minimized only when the predicted distribution matches the empirical data distribution. We use an unbiased two-sample estimator for the CRPS loss, summed over all grid points and variables:

$$\mathcal{L}_{\text{CRPS}} = \frac{1}{TN} \sum_{t=1}^T \sum_{n=1}^N \sum_{i=1}^{d_x} \frac{1}{2} \left(\left| \hat{X}_{n,i}^t - X_{n,i}^t \right| + \left| \check{X}_{n,i}^t - X_{n,i}^t \right| - \left| \hat{X}_{n,i}^t - \check{X}_{n,i}^t \right| \right) \quad (14)$$

where \hat{X}^t and \check{X}^t are two independent ensemble members (forecasts) generated by the model. Similarly to the deterministic case, we add a divergence loss term as in Eq. (8) computed on the predicted \hat{B}_x and \hat{B}_z components. The final training loss is the combination of these different objectives:

$$\mathcal{L} = \mathcal{L}_{\text{Var}} + \lambda_{\text{CRPS}} \mathcal{L}_{\text{CRPS}} + \lambda_{\text{Div}} \mathcal{L}_{\text{Div}}. \quad (15)$$

Computing the full probabilistic training loss requires rolling out three separate forecasts: one for the variational objective \mathcal{L}_{Var} (using latent samples drawn from the variational distribution q) and two for the CRPS objective $\mathcal{L}_{\text{CRPS}}$ (using samples from the latent map). This introduces a substantial computational overhead, but in practice the cost is manageable because the CRPS term is only included during the final stages of training.

4 Experiments

To evaluate our models, the Vlasiator simulations are causally split into training, validation, and test sets with durations of 12 minutes, 20 seconds, and 1 minute, respectively. This ensures that the evaluation tests for meaningful generalization into the future. We train both the deterministic Graph-FM and the probabilistic Graph-EFM models. All models are configured with latent dimensions $d_z = 256$ and $d_{\text{M2G}} = 128$. The processor consists of 12 processing layers. Graph-EFM is set to generate an ensemble size of 5. The models produce 30 s long forecasts during evaluation initialized from each simulation step in the test loader so that there are sufficient samples to calculate evaluation statistics on.

4.1 Training Details

All models are trained using the AdamW optimizer (Loshchilov & Hutter, 2019) with parameters $\beta_1 = 0.9$, $\beta_2 = 0.95$, a weight decay of 0.01, and an effective batch size of 32. The models are trained using bfloat16 mixed precision to save GPU memory. The full training schedules for both deterministic and probabilistic models are summarized in Table 4. The deterministic Graph-FM model is trained in three phases as detailed in the upper section of Table 4. The first 175 epochs use a learning rate of 10^{-3} with single-step unrolling. This is followed by 50 epochs at a reduced learning rate of

10^{-4} while gradually increasing the rollout length from 1 to 4 steps. Adding several unrolling steps to the loss has been shown to yield better long term performance (Lam et al., 2023) at the expense of increased computational complexity, which is why a majority of the training run is performed using single-step prediction. A final 25-epoch stage continues with $T = 4$ and introduces the magnetic divergence penalty with weight $\lambda_{\text{Div}} = 10$. The value for λ_{Div} is chosen such that \mathcal{L}_{Div} decreases nicely while the validation error of the predicted B_x and B_z components do not increase. This loss term is added only at the final stage so we can compare performance before and after its inclusion and explore different weight values at lower computational cost.

Table 4. Training schedules for the deterministic and probabilistic models.

Model	Epochs	Learning Rate	Unrolling T	λ_{KL}	λ_{CRPS}	λ_{Div}
Graph-FM	175	10^{-3}	1	-	-	0
	50	10^{-4}	1–4	-	-	0
	25	10^{-4}	4	-	-	10
Graph-EFM	100	10^{-3}	1	0	0	0
	50	10^{-3}	1	1	0	0
	50	10^{-4}	1–4	1	0	0
	25	10^{-4}	4	1	10^6	0
	25	10^{-4}	4	1	10^6	10^7

The probabilistic Graph-EFM model is trained in five stages as shown in the lower section of Table 4. In the first stage, we pretrain the network as a deterministic autoencoder by setting $\lambda_{\text{KL}} = 0$ and $\lambda_{\text{CRPS}} = 0$ for 100 epochs. This encourages q to encode meaningful information in the distribution over Z^t , and helps prevent the model from ignoring the latent variable and collapsing to deterministic forecasting (Oskarsson et al., 2024). In the second stage, we activate the variational term with $\lambda_{\text{KL}} = 1$ and train for 50 epochs on single-step predictions. The number of epochs is selected to give the training enough time to reach convergence. The third stage reduces the learning rate from 10^{-3} to 10^{-4} and increases the unroll length from 1 to 4 steps over 50 epochs to promote temporal stability. In the fourth stage, we introduce the CRPS loss with $\lambda_{\text{CRPS}} = 10^6$ for an additional 25 epochs. Finally, we add the magnetic divergence penalty with $\lambda_{\text{Div}} = 10^7$ for a 25-epoch fine-tuning stage. The λ_{CRPS} is chosen so that the SSR clearly increases without getting any visual artifacts, and the divergence weight is chosen in a similar way to the deterministic model so as to not increase the validation error for B_x and B_z while minimizing $\nabla \cdot \mathbf{B}$.

4.2 Computational Complexity

Table 5 summarizes the training and inference performance of the proposed models. Each training phase was conducted on 32 AMD MI250X GPUs. The CRPS stage (the final 50 epochs of Graph-EFM training) is by far the most computationally demanding training phase, requiring over 70 h for each model configuration. This is because computing the loss then requires rolling out two additional forecasts. Inference was benchmarked on a single AMD MI250X GPU and measured as the time it takes to complete one next-step prediction. For comparison, the physics-based Vlasiator simulation requires approximately 4–5 minutes on 100 AMD EPYC 7H12 CPUs with 64 cores each to simulate 1 s of physical time.

On a single GPU, the deterministic models predict the next step approximately 160 times faster than the original simulation running on 100 CPUs, while our probabilistic models are around 20 times faster with an ensemble size of 5. For this speed compar-

ison, one should note that the machine learning models are trained on ion VDF moments, whereas Vlasiator provides the full VDFs.

Table 5. Training and inference wall times for the Graph-FM and Graph-EFM models. Training was performed on 32 AMD MI250X GPUs, while inference times correspond to a single GPU. For Graph-EFM, the training time in parentheses indicate the time before CRPS fine-tuning, and inference times are reported per ensemble member.

Model	Parameters (M)	Training time (h)	Inference time (s)
Graph-FM	6.6	39.6	1.67
Graph-EFM	9.0	109 (35.3)	2.46

4.3 Metrics

To evaluate the performance of our forecasts, we use a set of standard metrics. For an ensemble forecast with M members (deterministic forecasts have $M = 1$), we denote the prediction for variable i at location n for a given sample s at time t as $\hat{X}_{n,i}^{s,t,m}$, with the corresponding ground truth being $X_{n,i}^{s,t}$. The Root Mean Squared Error (RMSE) is calculated by averaging the squared error over all S forecasts in the test set and all N grid locations:

$$\text{RMSE}_{t,i} = \sqrt{\frac{1}{SN} \sum_{s=1}^S \sum_{n=1}^N \left(\bar{X}_{n,i}^{s,t} - \hat{X}_{n,i}^{s,t} \right)^2} \quad (16)$$

$$\text{where } \bar{X}_{n,i}^{s,t} = \frac{1}{M} \sum_{m=1}^M \hat{X}_{n,i}^{s,t,m}. \quad (17)$$

The CRPS is calculated for ensemble forecasts to assess the overall quality of a probabilistic forecast by comparing the entire predictive distribution to the single ground truth observation. Lower values indicate better performance. We use a finite-sample estimate (Zamo & Naveau, 2018), computed as:

$$\text{CRPS}_{t,i} = \frac{1}{SN} \sum_{s=1}^S \sum_{n=1}^N \left(\frac{1}{M} \sum_{m=1}^M \left| \hat{X}_{n,i}^{s,t,m} - \bar{X}_{n,i}^{s,t} \right| - \frac{1}{2M(M-1)} \sum_{m=1}^M \sum_{m'=1}^M \left| \hat{X}_{n,i}^{s,t,m} - \hat{X}_{n,i}^{s,t,m'} \right| \right). \quad (18)$$

The ensemble spread quantifies the forecast uncertainty represented by the ensemble. It is defined as the root-mean-square deviation of the ensemble members from their ensemble mean:

$$\text{Spread}_{t,i} = \sqrt{\frac{1}{SMN} \sum_{s=1}^S \sum_{m=1}^M \sum_{n=1}^N \left(\bar{X}_{n,i}^{s,t} - \hat{X}_{n,i}^{s,t,m} \right)^2} \quad (19)$$

From this, the bias-corrected Spread–Skill-Ratio (SSR) is defined as

$$\text{SSR}_{t,i} = \sqrt{\frac{M+1}{M}} \frac{\text{Spread}_{t,i}}{\text{RMSE}_{t,i}} \quad (20)$$

An ensemble is considered well-calibrated when $\text{SSR} \approx 1$, indicating that the ensemble spread accurately reflects the forecast error (Fortin et al., 2014).

5 Results

5.1 Example Forecasts

Figure 2 presents example Graph-EFM forecasts for the plasma density ρ from four distinct Vlasiorator runs, corresponding to solar wind ion densities of 0.5, 1.0, 1.5, and 2.0 cm^{-3} (rows 1–4). As the upstream density increases, the bow shock is progressively compressed toward Earth. The model is trained to learn all four runs, and manages to successfully roll out physically consistent forecasts for each case individually. Regions of elevated ensemble spread align with dynamically active areas of the magnetosphere, indicating that forecast uncertainty is largest where the system is intrinsically more variable.

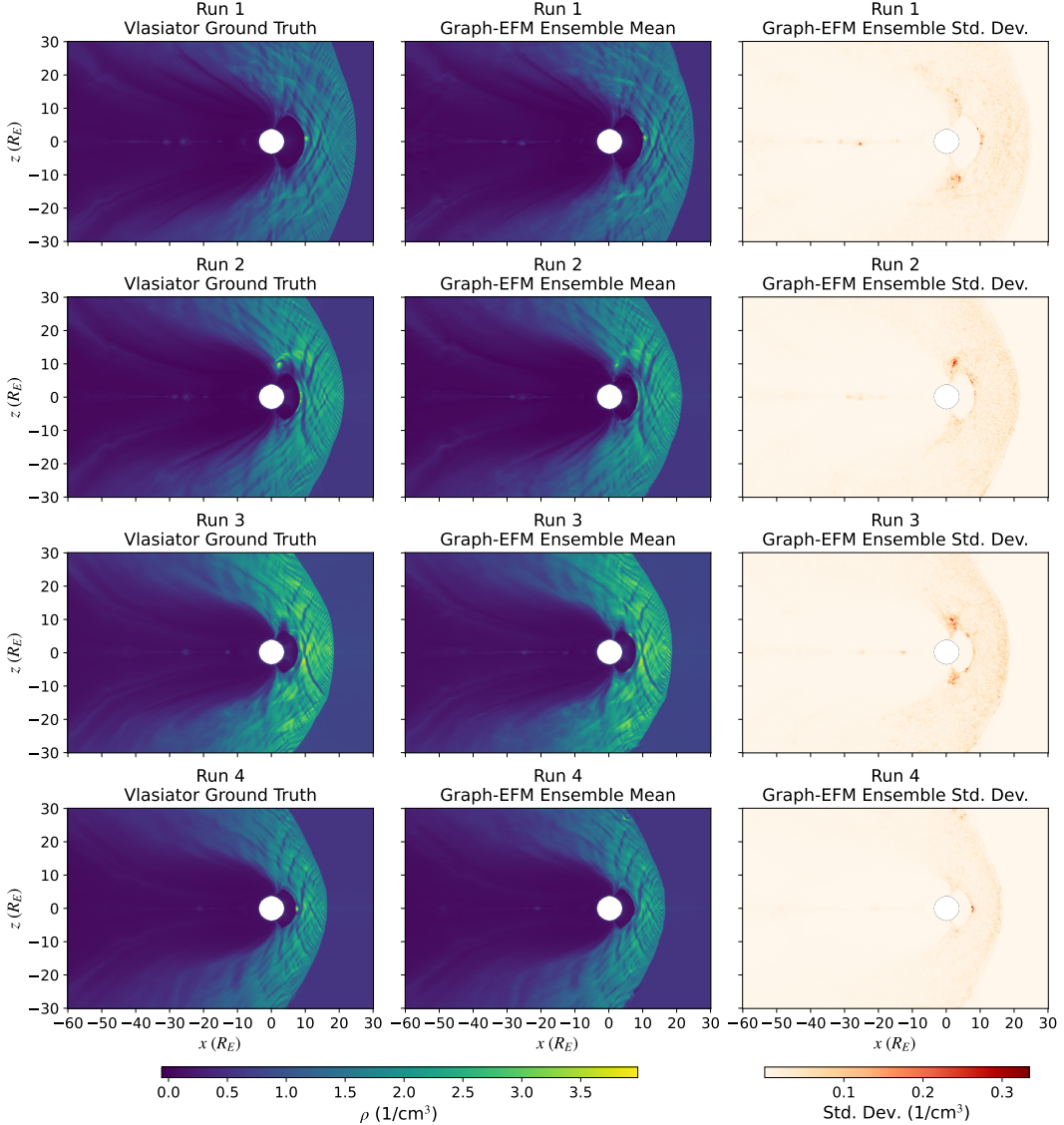


Figure 2. Example ρ Vlasiorator ground truth, Graph-EFM ensemble mean, and forecast uncertainty for each run at lead time $t = 30$ s for a forecast in the test set.

Mid-range values of the standard deviation (0.1–0.2) are attributed to the magnetosheath region, where it is almost homogeneously distributed, with a slight increase near the bow shock. The plasma dynamics in the magnetosheath are strongly turbulent and,

in the ion-kinetic regime, are largely governed by nonlinear interactions of electromagnetic waves driven by mirror and cyclotron instabilities. The behavior of the hybrid-Vlasov solver in this case is highly dependent on the numerical resolution (Dubart et al., 2020), and the resulting plasma state can be affected by numerical artifacts in velocity space that a fluid-like machine learning model is not aware of. Nevertheless, the model still reproduces wave activity with high accuracy, as evidenced by the correspondence of density striations in the magnetosheath observed in the left and central panels.

Peak values of the standard deviation (~ 0.3) are localized at the magnetopause and magnetotail current sheets. The dark red spots in the right column of Figure 2 correspond to high-density blobs, which are plasmoids generated by magnetic reconnection. These structures are transient, evolving on relatively short timescales and forming and dissipating in a stochastic manner. Notably, the maximum standard deviation is very high in the cusp regions for Runs 2 and 3, suggesting that the machine learning model encounters difficulties in accurately reproducing nonlinear processes in these dynamically complex regions, a limitation that is understandable given the inherently unpredictable nature of such phenomena.

The Supplementary Information provides plots for additional variables presented in the same format as Figure 2. Figures S1 and S2 show the magnetic field components B_x and B_z in the magnetotail and magnetopause current layers, respectively, where both exhibit uncertainty tied to their roles as reconnecting components. Figures S3, S4, and S5 display the electric field components E_x , E_y and E_z also associated with the reconnection process, while Figures S6 and S7 present the corresponding reconnection outflow velocities v_x (in the tail) and v_z (at the magnetopause). All these diagnostics consistently indicate elevated standard deviation values in regions dominated by magnetic reconnection.

5.2 Deterministic and Probabilistic Forecast Evaluation

The performance of all models is summarized in Figure 3, which shows the RMSE, CRPS, and SSR for lead times 1–30s. The metrics are calculated over the test set across the four runs such that forecasts are initialized at every timestep with an increment of 1s and rolled out for 30s. This yields an evaluation sample size of 116 forecasts in total. Here we focus on forecasting performance for B_x , E_x , v_x , and ρ , with results for the remaining variables provided in Supplementary Figures S8 and S9.

The RMSE measures the accuracy of the deterministic forecast (or ensemble mean), while the CRPS evaluates both accuracy and calibration of the full predictive distribution. Overall, the RMSE results are similar for Graph-FM and Graph-EFM. For comparison, we also include Graph-EFM before CRPS fine-tuning. RMSE, CRPS and SSR are all clearly improved after fine-tuning with the CRPS loss. Some of this may be attributed to the model just undergoing more optimization steps with the other loss terms active as well. The RMSE and CRPS curves increase almost linearly with lead time because forecast errors accumulate gradually under autoregressive rollout.

We evaluate the probabilistic performance of Graph-EFM using the SSR, a standard metric for assessing the reliability of ensemble forecasts. The SSR compares the ensemble spread, the ensemble's internal estimate of its own uncertainty, to the actual forecast error measured by the RMSE. Values below unity correspond to *underdispersive* ensembles, where the spread is too small relative to the forecast error, and values above unity indicate *overdispersion*. Across all selected variables and lead times from 1s to 30s, we find SSR values in the range 0.2–0.3. The SSR values are similar across variables and lead times, suggesting that Graph-EFM provides a stable but conservative estimate of forecast uncertainty across observables. Because the values are well below one the model clearly underestimate its own uncertainty. This is also a known characteristic of models trained primarily with a variational objective and in limited-area weather modeling

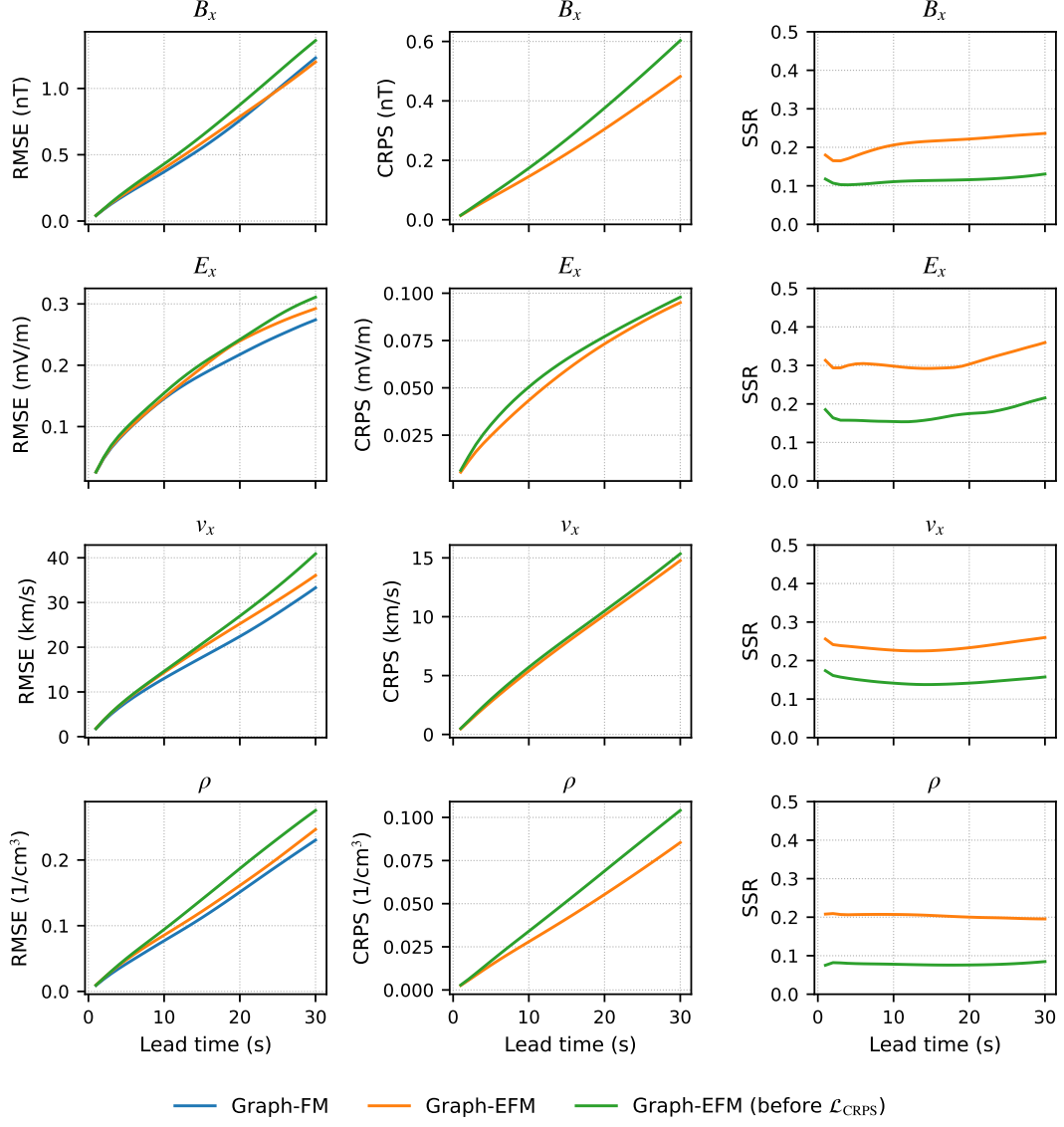


Figure 3. Forecast performance on the test set indicated by RMSE, CRPS, and SSR for all deterministic (Graph-FM) and probabilistic (Graph-EFM) models across variables B_x , E_x , v_x , and ρ for lead times 1–30 s.

(Oskarsson et al., 2024), analogous to our magnetospheric setup in space. The SSR lines are all quite flat with respect to lead time indicating that ensemble spread and RMSE grow at similar rates, producing a temporally consistent uncertainty estimate.

Interpreting these results requires considering the sources of uncertainty represented by the model. In probabilistic forecasting, uncertainties are typically divided into *epistemic* uncertainty, arising from limited data coverage or model capacity, and *aleatoric* uncertainty, corresponding to irreducible variability in the underlying system. For our hybrid-Vlasov simulations, there is effectively no intrinsic aleatoric uncertainty, as the system is governed by a fully deterministic set of equations. Consequently, the uncertainty relevant for emulation is epistemic, reflecting the model’s incomplete knowledge of the dynamics. In contrast, machine learning weather forecasting models are trained on decades of reanalysis data that also contain aleatoric variability from observational

noise injected into the simulation through data assimilation. In such settings, SSR values close to unity have been achieved (Alet et al., 2025).

5.3 Effect of Magnetic Divergence Penalty

To examine the influence of the magnetic divergence penalty, we compare multiple variants of Graph-FM and Graph-EFM trained with different divergence-loss weights. Figure 4 shows the RMSE for the magnetic field components B_x and B_z together with the mean absolute magnetic divergence $\langle |\nabla \cdot \mathbf{B}| \rangle$. The divergence penalty consistently reduces $\nabla \cdot \mathbf{B}$ across all models. For Graph-FM, weights of $\lambda_{\text{Div}} = 10$ and 100 yield progressively lower divergence, and $\lambda_{\text{Div}} = 1000$ pushes $\nabla \cdot \mathbf{B}$ well below that of the Vlasior reference. For Graph-EFM, a weight of $\lambda_{\text{Div}} = 10^7$ provides an improvement in divergence freeness without degrading RMSE of the affected magnetic field components. Larger values could be explored for the probabilistic model, but we did not perform an exhaustive sweep due to the substantial computational cost associated with multi-step CRPS fine-tuning. Here divergence loss was applied during the final stage of training to isolate its impact, but it could also be applied from the beginning of training as it is not an overly computationally expensive metric to optimize.

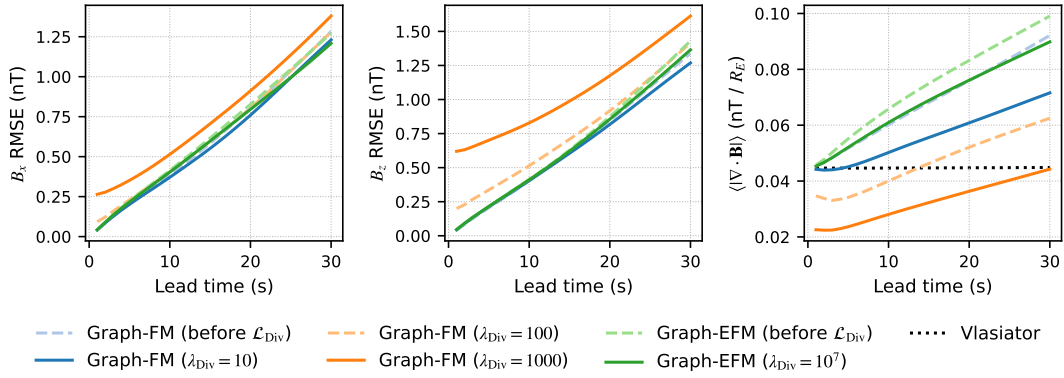


Figure 4. Effect of the magnetic divergence penalty. Shown are RMSE for B_x and B_z (left, center) and the mean absolute magnetic divergence over these fields (right) for Graph-FM and Graph-EFM models trained with different divergence-loss weights. The Vlasior reference is included as a black dashed line. Moderate penalty weights reduce divergence without affecting RMSE, whereas excessively large weights can push $\nabla \cdot \mathbf{B}$ below the physical reference and increase the error of the corresponding magnetic field components.

The chosen values $\lambda_{\text{Div}} = 10$ for Graph-FM and $\lambda_{\text{Div}} = 10^7$ for Graph-EFM were selected so that the validation RMSE for B_x and B_z remained stable during training. The test-set curves confirm this: for these weights, the magnetic field RMSE is essentially unchanged relative to the baseline with no divergence loss. However, when the divergence penalty becomes too strong, as in the Graph-FM ablations with $\lambda_{\text{Div}} = 1000$, the RMSE increases. This is consistent with the observation that these very large penalties drive $\nabla \cdot \mathbf{B}$ below the level present in the reference Vlasior simulation itself. However, we should note that the value of $\nabla \cdot \mathbf{B}$ depends on the discretization used to compute it; here we employ second-order central differences. Vlasior is physically divergence-free to numerical precision, but the training and evaluation here depend on this discretization of the divergence operator.

5.4 Ensemble Size Comparison

To assess how ensemble size affects predictive accuracy and uncertainty representation, we compare Graph-EFM models generating 2, 5, and 10 ensemble members. Figure 5 reports the normalized differences in RMSE, CRPS, and SSR relative to the 2-member ensemble, whose curves lie at zero by definition. For any metric m and ensemble size M , we plot the quantity $(m_M/m_2 - 1)$, so negative values indicate a reduction relative to the 2-member baseline. Lower RMSE and CRPS differences reflect improved forecast accuracy. In contrast, higher values for normalized SSR differences are beneficial because the ensembles are underdispersive, with SSR values below one for all three models, and higher spread is desired for the ensembles to be considered well-calibrated.

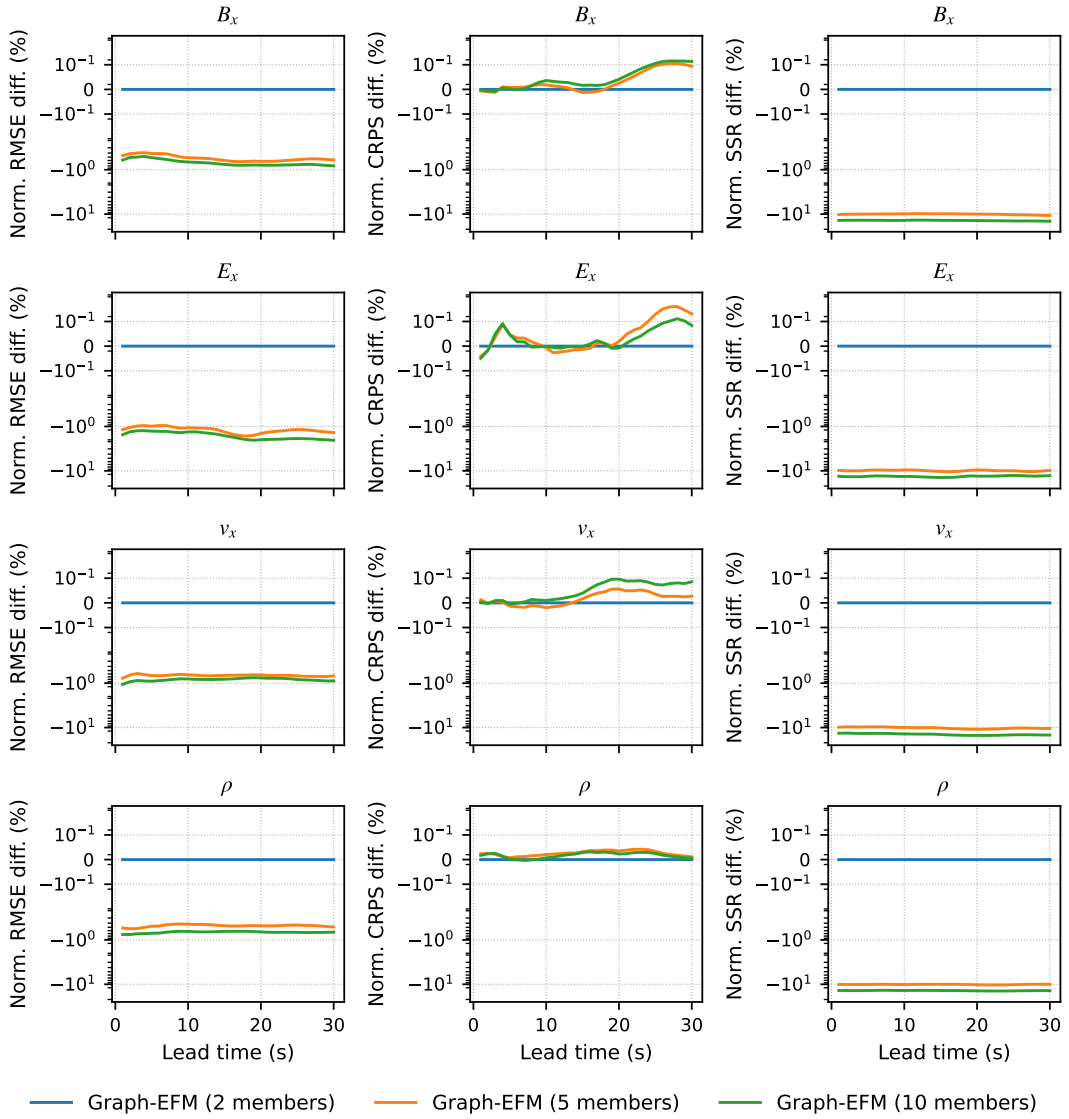


Figure 5. Normalized RMSE, CRPS, and SSR differences for Graph-EFM models using 2, 5, and 10 ensemble members. Values are reported relative to the 2-member ensemble (zero line). The y-axis has a symmetric logarithmic scale, that is linear between -0.2 and 0.2.

Increasing the number of ensemble members consistently reduces RMSE. This behavior reflects variance reduction in the ensemble mean: with more samples drawn from the latent distribution, the ensemble mean becomes a more accurate estimator of the expected plasma state. In contrast, the CRPS remains essentially unchanged across ensemble sizes, as the 5- and 10-member ensembles fluctuate by less than 0.1% relative to the 2-member ensemble. Because the CRPS evaluates the underlying predictive distribution rather than the number of samples drawn from it, its expected value is largely independent of ensemble size once the distribution is adequately represented.

The SSR metric, by comparison, decreases with increasing ensemble size. This could stem from a finite-sample effect, where occasional large pairwise differences increase spread, and larger ensembles provide a more stable estimate of the predictive variance while also reducing the RMSE of the ensemble mean.

5.5 Autoregressive Step Size Comparison

To assess how the autoregressive stride affects forecast skill, we train Graph-FM models with $\Delta t = 1\text{ s}$, 2 s , and 3 s . The training data for the 2 s and 3 s models is obtained by temporal subsampling, reducing the number of available training snapshots by factors of two and three, respectively. To ensure a fair comparison, the number of optimization steps is held constant across models: the 2 s and 3 s variants are trained for proportionally more epochs so that each model performs an equal number of gradient updates.

Despite being exposed to fewer unique training samples, the 2 s and 3 s models accumulate less forecast error than the 1 s model across all variables in Figure 6, with the exception of a few early lead times. This improvement arises because longer autoregressive strides require fewer rollout steps to reach a given physical lead time, thereby reducing the compounding of one-step prediction errors. This behavior suggests that space-weather emulators can benefit from larger step sizes if long term forecast is the goal. Step sizes *much* larger than here are certainly an option for operational MHD models that natively run with larger time steps and where longer term data is available. This is also seen in atmospheric weather emulation, where models learn from 6-hourly mean aggregated reanalysis fields even though the underlying simulators run with much smaller time steps. Data-driven weather models have also been shown to continuously accumulate less error for 15-day forecasts as the step size is increased from 1 h to 24 h (Bi et al., 2023).

5.6 Power Spectra of Forecasted Fields

To further assess how well the models reproduce the spatial variability of the simulated plasma and field quantities, we compute the isotropic two-dimensional power spectra of each variable at several forecast lead times. For a given field $f(x, z)$, the power spectrum $P(k)$ is defined as the azimuthally averaged squared modulus of its two-dimensional Fourier transform,

$$P(k) = \left\langle \left| \hat{f}(k_x, k_z) \right|^2 \right\rangle_{(k_x, k_z): \sqrt{k_x^2 + k_z^2} = k}, \quad (21)$$

where k_x and k_z are the wavenumbers in the x - and z -directions, respectively, and $k = \sqrt{k_x^2 + k_z^2}$ denotes the radial wavenumber. The wavenumber k has units of R_E^{-1} and corresponds to spatial structures of characteristic scale $\lambda = \frac{2\pi}{k}$. Hence, small k represents large-scale (global) structures, while large k corresponds to finer, small-scale variations. All spectra are computed from 50 s rollouts initialized at the start of the test segment for each of the four simulation runs, and then averaged across runs.

The vertical axis in Figures 7 shows the power $P(k)$, which measures the contribution of each spatial scale to the total variance of the field. Each subplot corresponds to one physical variable (rows) at a given forecast time (columns). The solid blue and

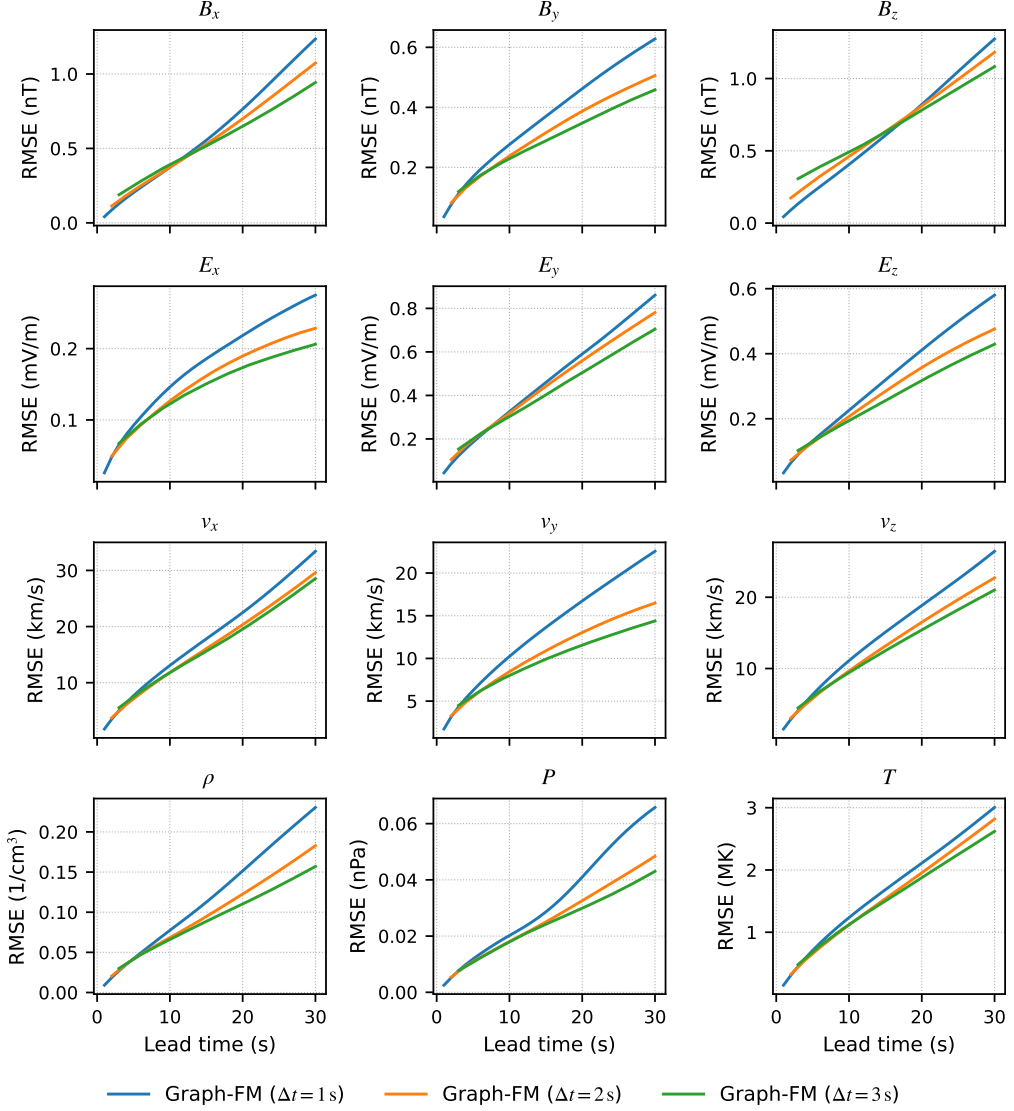


Figure 6. RMSE as a function of lead time for Graph-FM models trained with autoregressive step sizes of 1, 2, and 3 s. Larger step sizes reduce temporal error accumulation despite training on less data.

orange curves indicate the spectra of the Graph-FM and Graph-EFM ensemble mean forecasts, respectively, while the black dashed curve shows the reference spectrum computed from the Vlasiator simulation. The models are evaluated at four lead times ($t = 1$ s, 10 s, 30 s, and 50 s), allowing assessment of how well small- and large-scale energy distributions are preserved during the forecast. Supplementary Figure S10 shows the power spectra of the remainder of the variables.

Both models reproduce the large-scale structure of the power spectra well, particularly for the magnetic field component B_x , whose spectrum closely matches the Vlasiator reference at all lead times. For the remaining variables (E_x , v_x , ρ , P , and T), differences emerge primarily at higher wavenumbers. Graph-EFM maintains spectra that remain close to the reference for most scales, with deviations confined to the very highest wavenumbers indicating that it loses some fine-scale details over time. Graph-FM on

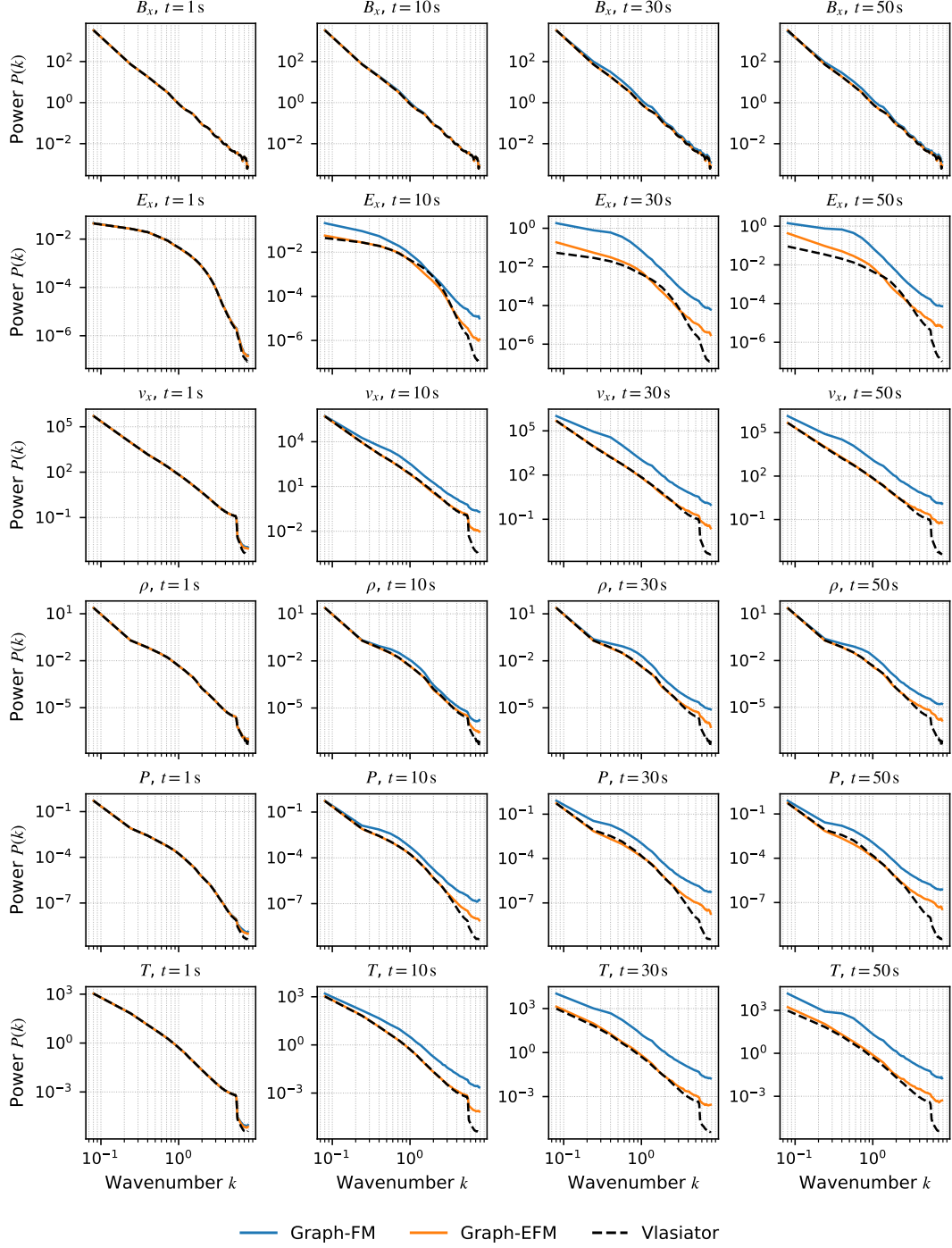


Figure 7. Spatial power spectra of B_x , E_x , v_x , ρ , P and T . Each panel shows the isotropic power $P(k)$ versus wavenumber k , comparing Graph-FM and Graph-EFM forecasts with the Vlasiator ground truth at forecast lead times of $t = 1, 10, 30$, and 50 s.

the other hand show elevated power across a wide band of high wavenumbers. It is a known phenomenon that machine learning forecast models trained with an MSE objective have a tendency to produce blurred forecast at higher lead times (Lam et al., 2023).

An exception to this trend is the B_x component in Figure 7 and the B_z component in Figure S10, whose spectra are reproduced with remarkable accuracy by both models at all lead times. This behavior can potentially be attributed to the intrinsic dipole magnetic field. In the inner magnetospheric region, the dipole field dominates the magnetic configuration and is orders of magnitude stronger than the perturbation field generated by magnetospheric dynamics, particularly close to the inner boundary, and this background field is comparatively static in time. As a result, B_x and B_z then inherit a strong, slowly varying large-scale structure that may stabilize their spectral content and makes it easier to reproduce accurately, even at longer lead times.

5.7 Correlation with Simulation

Lastly, to assess forecast quality beyond aggregate error metrics, we analyze the pointwise correlation between predicted and true fields using prediction-versus-truth density plots. The analysis is based on the same 50 s autoregressive rollouts initialized at the start of the test segment for each of the four simulation runs that were used in the spectral evaluation. For the results shown here, all grid points from the four forecasts are pooled for each physical variable and lead time.

Figure 8 shows the density plots for the Graph-EFM model at lead time $t = 30$ s, displayed separately for each of the twelve physical variables. Each panel presents a two-dimensional histogram of predicted values against the corresponding Vlasior reference values, with colors indicating point density on a logarithmic scale. The dashed black line denotes the ideal one-to-one relationship, the solid white line shows a least-squares fit, and the annotated Pearson correlation coefficient summarizes the linear association between forecast and ground truth.

Across most variables, the distributions remain concentrated along the one-to-one line, indicating that Graph-EFM preserves the dominant spatial structure of the simulated fields even at this extended lead time. As expected under autoregressive rollout, the distributions broaden relative to earlier lead times (see Figures S11 and S12 for lead times $t = 10$ s and 50 s, respectively), reflecting the gradual accumulation of forecast uncertainty.

At longer lead times, a pronounced vertical band of density appears around zero true values for B_y , E_x , E_z , and v_y . This pattern arises because these components are close to zero over large fractions of the simulation domain. The reason for this is that in the 2D + 3V hybrid-Vlasov configuration, spatial variations are restricted to the x - z plane, i.e. $\partial/\partial y = 0$, which imposes an approximate symmetry in the out-of-plane direction. As a result, the dominant magnetospheric dynamics are primarily in-plane, producing strong B_x and B_z , while the out-of-plane magnetic field B_y is only generated through localized current systems and therefore remains small in most regions.

The same geometric constraint also shapes the electric field. In the hybrid model it is given by the generalized Ohm's law:

$$\mathbf{E} = -\mathbf{v} \times \mathbf{B} + \frac{\mathbf{J} \times \mathbf{B}}{ne}, \quad (22)$$

where the first term represents the convective electric field and the second the Hall contribution. Because the symmetry implies no sustained force balance in the y direction, the mean bulk flow satisfies $\langle v_y \rangle \approx 0$ over most of the domain, and the magnetic field is likewise predominantly in-plane with $B_y \approx 0$ except in localized regions. Under these conditions, the convective term reduces to:

$$-\mathbf{v} \times \mathbf{B} = (-(v_y B_z - v_z B_y), -(v_z B_x - v_x B_z), -(v_x B_y - v_y B_x)) \approx (0, E_y, 0), \quad (23)$$

so that it contributes mainly to the out-of-plane electric field component E_y .

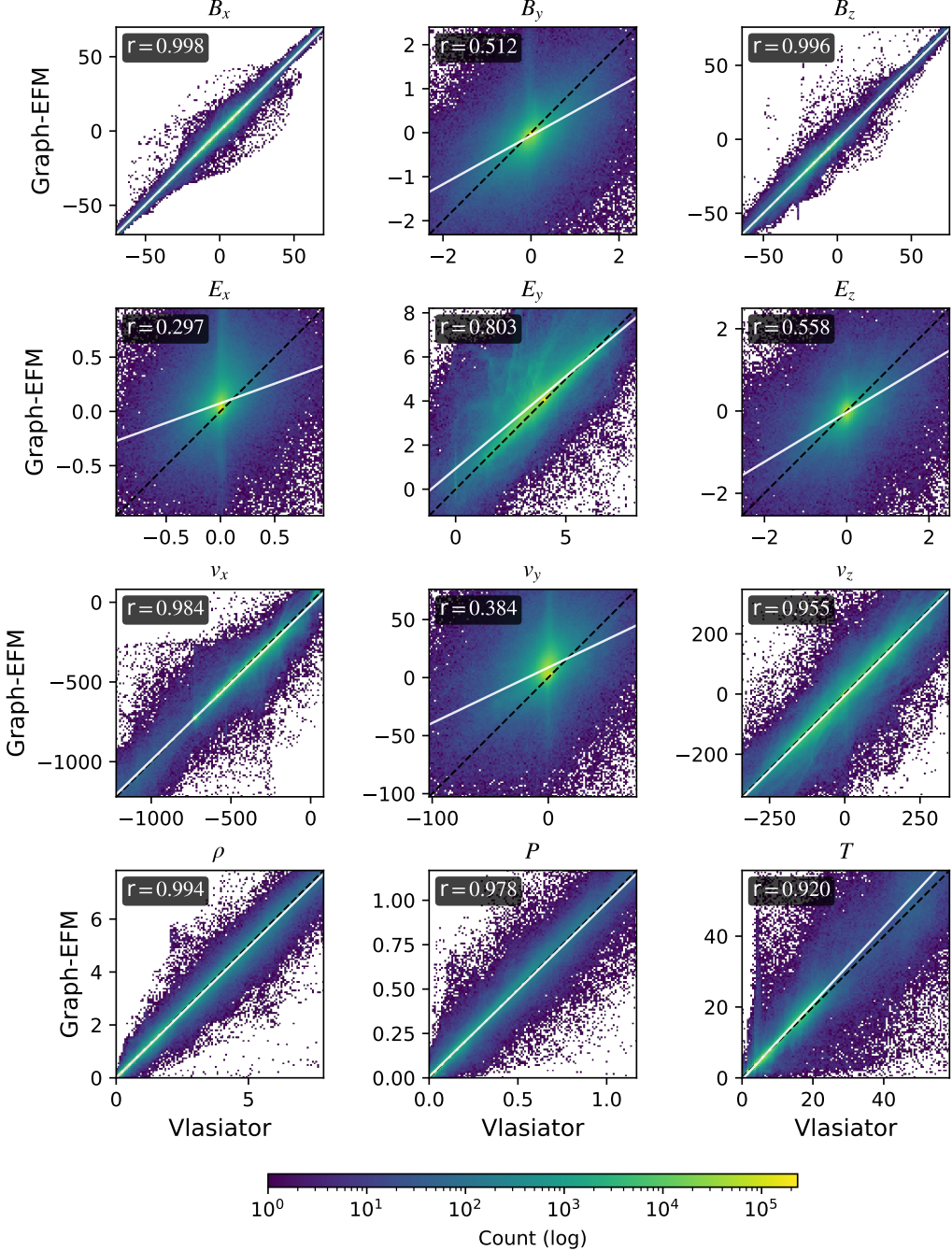


Figure 8. Two-dimensional density plots illustrating the relationship between predicted and ground truth values for Graph-EFM at a lead time of $t = 30$ s are shown for each physical variable. Each panel aggregates results from four forecasts. Colors represent logarithmic point density, the dotted line indicates the one-to-one relation, the solid line shows the least-squares fit, and the annotated Pearson coefficient summarizes linear correlation.

The in-plane components E_x and E_z therefore arise primarily from the Hall term $\mathbf{J} \times \mathbf{B}/(ne)$, which becomes significant in regions where the current is not aligned with the magnetic field, such as thin current sheets, reconnection sites, and boundary layers.

These processes are spatially localized, explaining why E_x and E_z remain comparatively weak over most of the domain.

These physical motivations explains why a large fraction of grid points are zero for the variables B_y , E_x , E_z , and v_y , and even modest prediction variability around zero leads to a visually prominent vertical band in the density plots comparing prediction with ground truth. The impact of this effect increases with forecast horizon: at lead time $t = 10\text{s}$ the distributions remain tightly aligned with the diagonal and Pearson correlations exceed 0.9 even for these more challenging variables, whereas by $t = 30\text{s}$ correlations drop to about 0.4–0.5 and the vertical band becomes more pronounced. At $t = 50\text{s}$, correlations further decrease to 0.1–0.25. The remaining observables exhibit consistently high correlations, many of them exceeding 0.9 at lead times of 30 s and 50 s.

The gradual buildup of unintended nonzero values is most clearly visible for E_x in Figure S3, particularly in the bow shock of Run 1. Given the strongly zero-peaked target distributions of B_y , E_x , E_z , and v_y , small unbiased prediction errors around zero can accumulate under autoregressive rollout. This can lead to the observed biases, also seen in the power spectra for the E_x in Figure 7 as a drift from the ground truth line, even at smaller wavenumbers.

Zero-inflated observables of this type are relatively uncommon in neural-emulator benchmarks, and improved treatment could involve explicitly enforcing near-zero structure, for example by predicting signed log-magnitudes, or using mixture models with a point mass at zero. A practical solution in our case, is to just move on to simulations with tree spatial dimensions, because then the symmetry constraint $\partial/\partial y = 0$ is removed, and the same components are no longer suppressed, meaning we get rid of the near-degenerate distributions of B_y , E_x , E_z , and v_y .

6 Discussion

In this work, we presented neural surrogates of global hybrid-Vlasov simulations with built-in uncertainty quantification. The emulation, however, takes place on a 2D plane and on a regular grid. Global hybrid-Vlasov models are in general computationally so demanding that mesh refinement becomes essential, especially when modeling the full three spatial dimensions. This allows for higher spatial resolution in critical regions, like the bow shock and the magnetotail reconnection site near Earth, while using lower resolution in less important areas such as inflow and outflow boundaries (Ganse et al., 2023) resulting in irregular data structures. GNNs have been shown to work well also for irregular domains where they have been used for predicting the mean flow (Mousavi et al., 2025) as well as the full distribution (Valencia et al., 2025) of PDE systems. Recently physics-motivated adaptive mesh refinement has also been implemented for Vlasitator (Kotipalo et al., 2024), where the refinement is controlled directly by physical conditions. These developments present additional interesting challenges for neural emulators.

Here we predict the spatiotemporal evolution of velocity space moments of the ion VDFs, which Vlasitator solves fully. A natural progression would be to forecast the entire VDFs over time, rather than just their moments. Here one could take inspiration from previous work on emulating gyrokinetic simulations (Paischer et al., 2025), where a hierarchical vision transformer was used for evolving the full 5D dynamics. Further extending to three spatial dimensions is required for it to be physically complete, where early studies have demonstrated that neural emulators can scale effectively to large 3D fluid simulations (Luo et al., 2025; Molinaro et al., 2025; Holzschuh et al., 2025). Hence, a full hybrid-Vlasov emulator would have to model a 3D + 3V, or six-dimensional, system to reproduce the complete phase-space dynamics.

Producing sufficient training data to create a useful 3D + 3V kinetic-scale neural emulator would require immense computational resources. Advances in speeding up Vlasov are taking place that could alleviate this issue to some extent. For example, the previously mentioned adaptive mesh refinement is one important improvement. Further ongoing work on porting the simulation code to support running on GPUs (Battarbee et al., 2025) is a necessary long term investment for speeding up the simulation as hardware accelerators continues to become more powerful. Lastly, using machine learning to compress the VDFs (Papadakis et al., 2025) could offer a promising way to alleviate the most computationally demanding part of the simulation.

In terms of improving the probabilistic forecasts, alternative diffusion-based (Price et al., 2025) and CRPS-based (Alet et al., 2025) models have also demonstrated skillful ensemble weather forecasts, even with finetuning on few autoregressive steps. However, compared to diffusion models, Graph-EFM is a faster model, as a single forward pass per member is sufficient, whereas diffusion models require multiple passes due to their iterative refinement process. On the other hand, CRPS-based ensemble weather forecasting models trained by matching only marginal distributions through a CRPS loss function, also allow for sampling ensemble members in a single forward pass through the network (Alet et al., 2025). Such an approach could provide an interesting alternative to the one presented here. The training schedule can further be made a bit simpler compared to the Graph-EFM variational framework (Larsson et al., 2025).

A further limitation of neural emulators, is that they generally struggle with error accumulation on long rollouts, causing simulated trajectories to diverge. This happens because the model gradually operates out of distribution with each autoregressive step. To combat this, techniques based on diffusion models have been proposed to do iterative spectral refinement (Lippe et al., 2023), or transport a system moving into regions of low probability back to equilibrium (Pedersen et al., 2025). Another promising diffusion-based method to tackle cumulative error for probabilistic forecasts involves training models to forecast a future state in a single step while ensuring the temporal consistency of the forecast (Andrae et al., 2025), which can be used to provide continuous time ensemble forecasts.

Another central challenge for neural emulators is how to enforce physical consistency. In this study, we apply a soft constraint in the loss function to encourage divergence-freeness of the magnetic field. The public dataset accompanying this work can further enable the development of hybrid-Vlasov emulators that more faithfully obey underlying physical constraints. Recent advances have proposed alternative strategies for enforcing hard physical constraints directly within generative models, where conservation laws are formulated in their integral form and satisfied through probabilistic control of variance (Hansen et al., 2023). Alternatively, inference-time correction frameworks have been introduced to impose arbitrary nonlinear constraints on pretrained flow-based models by guiding their generative trajectories toward physics-consistent states (Utkarsh et al., 2025).

A recent trend is also to attempt learning across systems to facilitate transfer of information between them. To facilitate such approaches, community initiatives are gathering diverse physics simulations to create large-scale datasets for machine learning (Ohana et al., 2024; Tali et al., 2024). These can then be used to train foundation models, that learn dynamics from multiple physical systems (Nguyen et al., 2025; McCabe et al., 2025). Similar efforts have also taken place for weather (Bodnar et al., 2025), solar activity (Roy et al., 2025), and astronomy (Parker et al., 2025) to name a few examples. Space weather data as presented here could be a valuable addition to these growing scientific datasets. Likewise, space weather prediction models can *potentially* be improved by finetuning foundation models, allowing them to leverage insights from various physical domains and generalize better.

Lastly, we will comment a few words on the state of data-driven space weather forecasting. In comparison to terrestrial weather, space weather is said to significantly lag behind in modeling, data, forecast accuracy, and operational infrastructure (Guerra et al., 2020). Realizing the full benefits of data-driven forecasting, requires long and high-quality training datasets, as demonstrated in atmospheric machine learning weather prediction (Ben Bouallegue et al., 2024), and when machine learning models are trained on simulations augmented using data assimilation, they are even able to *outperform* purely physics-based forecasts in terms of accuracy. The reason for this is that the training targets represent states that have been systematically corrected toward observations. In space weather, data assimilation is not yet standard practice, but in the instances where it has been applied, significant improvements in the representation of the solar wind have been reported (M. Lang et al., 2017, 2021), even when mimicking an operational setting (Turner et al., 2023).

The availability of open, long-term space-weather reanalyses spanning multiple solar cycles would therefore be highly valuable. Such datasets could enable machine-learning models to learn the diverse conditions that exist in reality, and also facilitate the use of larger prediction time steps, thereby mitigating the error accumulation inherent to autoregressive forecasting. A particularly promising direction for neural surrogates in space weather prediction is the emulation of heliospheric MHD models. Recent work has shown that neural operators can outperform a reduced-physics model for propagating the radial solar-wind velocity field from 30 solar radii to 1 AU (Mansouri et al., 2025). Further neural enhancements of ambient solar-wind modeling (Mayank et al., 2025) could complement this approach at the inner coronal boundary commonly used to drive heliospheric MHD simulations, and together enable the development of a fully differentiable forecasting pipeline from the Sun to near-Earth space. Together with a working data-assimilation scheme applied to the training data, and ensemble forecasting capability as presented here, these developments could give rise to a whole new generation of space weather forecasting systems that are both faster and more accurate than traditional ones.

7 Conclusion

In this work, we developed graph-based neural emulators that reproduce the short-term evolution of plasma and electromagnetic fields in a global hybrid-Vlasov simulation while running orders of magnitude faster than the underlying first-principles model. Using a set of Vlasiator runs that span a controlled range of particle number densities and Alfvén Mach numbers, we showed that the proposed approach provides accurate forecasts for the observables that govern near Earth space dynamics.

Both deterministic and probabilistic formulations were evaluated. The deterministic model provides fast, single-point next step predictions, while the probabilistic model generates ensembles of future states and supplies meaningful uncertainty information. Such capability is actively sought in space weather forecasting systems and in plasma simulation more broadly. CRPS based fine tuning improves the calibration of ensemble predictions. A soft divergence penalty further reduces magnetic field divergence without degrading predictive performance. Power spectral analysis confirms that the emulators capture the dominant large scale structures of the hybrid-Vlasov system, with small scale deviations consistent with autoregressive error accumulation.

Another central contribution of this study is the release of a hybrid-Vlasov dataset comprised of electromagnetic fields and the plasma moments provided as easily accessible Zarr stores, that enables the broader machine learning community to work with plasma simulations that incorporate ion-kinetic effects at global scale. The open codebase for the forecasting methods is further compatible with developments in machine learning-based atmospheric weather prediction that can help translate advances in a very active field of research to the domain of space weather.

The results demonstrate that neural emulators can serve as practical surrogates for computationally intensive kinetic models and can support rapid forecasting and uncertainty quantification. Extending these approaches to longer forecast horizons, three dimensional domains, a wider range of solar wind driving conditions, and potentially the prediction of full VDFs represents promising directions for future work in machine learning-based plasma and space weather emulation.

Open Research Section

The source code used to train and evaluate the machine-learning models is openly available on GitHub (Holmberg, 2025) under MIT open-source license. The training data was produced using Vlasiator version 5.3.1 (Pfau-Kempf et al., 2024), and is hosted on Hugging Face (Zaitsev et al., 2025) under Creative Commons Attribution 4.0 license.

Conflict of Interest

The authors declare there are no conflicts of interest for this manuscript.

Acknowledgments

This work was funded by the Research Council of Finland grants 361901 and 361902 (FAISER). Vlasiator was developed with support from the European Research Council's starting grant 200141 (QuESpace) and consolidator grant 682068 (PRESTISSIMO). D.H. acknowledges support from the Fulbright-KAUTÉ Foundation Award for conducting research at UC Santa Barbara. D.H. wishes to thank Joel Oskarsson and Erik Larsson for helpful discussions on probabilistic weather modeling. M.P. acknowledges Research Council of Finland grant 352846 (Centre of Excellence in Research of Sustainable Space). Computing resources were provided by the LUMI supercomputer, owned by the EuroHPC Joint Undertaking and hosted by CSC-IT Center for Science.

References

Alet, F., Price, I., El-Kadi, A., Masters, D., Markou, S., Andersson, T. R., ... Battaglia, P. (2025). Skillful joint probabilistic weather forecasting from marginals. *arXiv preprint arXiv:2506.10772*.

Andrae, M., Landelius, T., Oskarsson, J., & Lindsten, F. (2025). Continuous ensemble weather forecasting with diffusion models. In *International conference on learning representations*.

Baker, D. (1998). What is space weather? *Advances in Space Research*, 22(1), 7–16.

Baker, D., Daly, E., Daglis, I., Kappenman, J. G., & Panasyuk, M. (2004). Effects of space weather on technology infrastructure. *Space Weather*, 2(2).

Battaglia, P., Pascanu, R., Lai, M., Jimenez Rezende, D., et al. (2016). Interaction networks for learning about objects, relations and physics. In *Advances in neural information processing systems*.

Battarbee, M., Papadakis, K., Ganse, U., Hokkanen, J., Kotipalo, L., Pfau-Kempf, Y., ... Palmroth, M. (2025). Porting the grid-based 3D+3V hybrid-Vlasov kinetic plasma simulation Vlasiator to heterogeneous GPU architectures. In *Journal of physics: Conference series* (Vol. 2997, p. 012010).

Ben Bouallegue, Z., Clare, M. C., Magnusson, L., Gascon, E., Maier-Gerber, M., Janoušek, M., ... others (2024). The rise of data-driven weather forecasting: A first statistical assessment of machine learning-based weather forecasts in an operational-like context. *Bulletin of the American Meteorological Society*, 105(6), E864–E883.

Bi, K., Xie, L., Zhang, H., Chen, X., Gu, X., & Tian, Q. (2023). Accurate medium-range global weather forecasting with 3D neural networks. *Nature*, 619(7970), 533–538.

Bodnar, C., Bruinsma, W. P., Lucic, A., Stanley, M., Allen, A., Brandstetter, J., ... others (2025). A foundation model for the Earth system. *Nature*, 641(8065), 1180–1187.

Bolduc, L. (2002). GIC observations and studies in the Hydro-Québec power system. *Journal of Atmospheric and Solar-Terrestrial Physics*, 64(16), 1793–1802.

Brackbill, J. U., & Barnes, D. C. (1980). The effect of nonzero $\nabla \cdot \mathbf{B}$ on the numerical solution of the magnetohydrodynamic equations. *Journal of Computational Physics*, 35(3), 426–430.

Camporeale, E., Chu, X., Agapitov, O., & Bortnik, J. (2019). On the generation of probabilistic forecasts from deterministic models. *Space Weather*, 17(3), 455–475.

Carey, N., Zanisi, L., Pamela, S., Gopakumar, V., Omotani, J., Buchanan, J., ... Setinek, P. (2025). Neural operator surrogate models of plasma edge simulations: feasibility and data efficiency. *Nuclear Fusion*, 65(10), 106010.

Carvalho, D. D., Ferreira, D. R., & Silva, L. O. (2024). Learning the dynamics of a one-dimensional plasma model with graph neural networks. *Machine Learning: Science and Technology*, 5(2), 025048.

Chen, T., Xu, B., Zhang, C., & Guestrin, C. (2016). Training deep nets with sublinear memory cost. *arXiv preprint arXiv:1604.06174*.

Dimmock, A. P., Rosenqvist, L., Hall, J.-O., Viljanen, A., Yordanova, E., Honkonen, I., ... Sjöberg, E. (2019). The GIC and geomagnetic response over Fennoscandia to the 7–8 September 2017 geomagnetic storm. *Space Weather*, 17(7), 989–1010.

Dubart, M., Ganse, U., Osmane, A., Johlander, A., Battarbee, M., Grandin, M., ... Palmroth, M. (2020). Resolution dependence of magnetosheath waves in global hybrid-Vlasov simulations. *Annales Geophysicae Discussions*, 2020, 1–23.

Falcon, W., Borovec, J., & The PyTorch Lightning team. (2024). *PyTorch Lightning*. Zenodo. doi: 10.5281/zenodo.1325426

Fortin, V., Abaza, M., Anctil, F., & Turcotte, R. (2014). Why should ensemble spread match the RMSE of the ensemble mean? *Journal of Hydrometeorology*, 15(4), 1708–1713.

Ganse, U., Koskela, T., Battarbee, M., Pfau-Kempf, Y., Papadakis, K., Alho, M., ... others (2023). Enabling technology for global 3D + 3V hybrid-Vlasov simulations of near-Earth space. *Physics of Plasmas*, 30(4).

Glocer, A., Fok, M., Meng, X., Toth, G., Buzulukova, N., Chen, S., & Lin, K. (2013). CRCM + BATS-R-US two-way coupling. *Journal of Geophysical Research: Space Physics*, 118(4), 1635–1650.

Gneiting, T., & Raftery, A. E. (2007). Strictly proper scoring rules, prediction, and estimation. *Journal of the American Statistical Association*, 102(477), 359–378.

Gopakumar, V., Pamela, S., Zanisi, L., Li, Z., Gray, A., Brennand, D., ... others (2024). Plasma surrogate modelling using fourier neural operators. *Nuclear Fusion*, 64(5), 056025.

Gubby, R., & Evans, J. (2002). Space environment effects and satellite design. *Journal of Atmospheric and Solar-Terrestrial Physics*, 64(16), 1723–1733.

Guerra, J. A., Murray, S. A., & Doornbos, E. (2020). The use of ensembles in space weather forecasting. *Space Weather*, 18(2), e2020SW002443.

Guerra, J. A., Pulkkinen, A., & Uritsky, V. M. (2015). Ensemble forecasting of major solar flares: First results. *Space Weather*, 13(10), 626–642.

Hansen, D., Maddix, D. C., Alizadeh, S., Gupta, G., & Mahoney, M. W. (2023). Learning physical models that can respect conservation laws. In *International conference on machine learning*.

Hoilijoki, S., Ganse, U., Pfau-Kempf, Y., Cassak, P. A., Walsh, B. M., Hietala, H., ... Palmroth, M. (2017). Reconnection rates and X line motion at the magnetopause: Global 2D-3V hybrid-Vlasov simulation results. *Journal of Geophysical Research: Space Physics*, 122(3), 2877–2888.

Holmberg, D. (2025). *fmihpc/spacecast*. GitHub. Retrieved from <https://github.com/fmihpc/spacecast> (Open source software, MIT License)

Holmberg, D., Zaitsev, I., Alho, M., Bouri, I., Franssila, F., Jeong, H., ... Roos, T. (2025). Graph-based neural space weather forecasting. In *NeurIPS 2025 workshop on machine learning and the physical sciences*.

Holzschuh, B., Kohl, G., Redinger, F., & Thuerey, N. (2025). P3D: Scalable neural surrogates for high-resolution 3D physics simulations with global context. *arXiv preprint arXiv:2509.10186*.

Honkonen, I., van de Kamp, M., Hoppe, T., & Kauristie, K. (2022). Over 20-year global magnetohydrodynamic simulation of Earth's magnetosphere. *Space Weather*, 20(11), e2022SW003196.

Janhunen, P., Palmroth, M., Laitinen, T., Honkonen, I., Juusola, L., Facskó, G., & Pulkkinen, T. I. (2012). The GUMICS-4 global MHD magnetosphere-ionosphere coupling simulation. *Journal of Atmospheric and Solar-Terrestrial Physics*, 80, 48–59.

Kataoka, R., Nakamizo, A., Nakano, S., & Fujita, S. (2024). Machine learning-based emulator for the physics-based simulation of auroral current system. *Space Weather*, 22(1), e2023SW003720.

Keisler, R. (2022). Forecasting global weather with graph neural networks. *arXiv preprint arXiv:2202.07575*.

Kelebek, H. S., Wolniewicz, L. M., Vergalla, M. D., Mestici, S., Acciarini, G., Poduval, B., ... others (2025). IonCast: A deep learning framework for forecasting ionospheric dynamics. In *NeurIPS 2025 workshop on machine learning and the physical sciences*.

Kingma, D. P., & Welling, M. (2014). Auto-encoding variational Bayes. In *International conference on learning representations*.

Kochkov, D., Smith, J. A., Alieva, A., Wang, Q., Brenner, M. P., & Hoyer, S. (2021). Machine learning-accelerated computational fluid dynamics. *Proceedings of the National Academy of Sciences*, 118(21), e2101784118.

Kotipalo, L., Battarbee, M., Pfau-Kempf, Y., & Palmroth, M. (2024). Physics-motivated cell-octree adaptive mesh refinement in the Vlasiator 5.3 global hybrid-Vlasov code. *Geoscientific Model Development*, 17(16), 6401–6413.

Lam, R., Sanchez-Gonzalez, A., Willson, M., Wirnsberger, P., Fortunato, M., Alet, F., ... others (2023). Learning skillful medium-range global weather forecasting. *Science*, 382(6677), 1416–1421.

Lang, M., Browne, P., Van Leeuwen, P. J., & Owens, M. (2017). Data assimilation in the solar wind: Challenges and first results. *Space Weather*, 15(11), 1490–1510.

Lang, M., Witherington, J., Turner, H., Owens, M. J., & Riley, P. (2021). Improving solar wind forecasting using data assimilation. *Space Weather*, 19(7), e2020SW002698.

Lang, S., Alexe, M., Clare, M. C., Roberts, C., Adewoyin, R., Bouallègue, Z. B., ... others (2024). AIFS-CRPS: Ensemble forecasting using a model trained with a loss function based on the continuous ranked probability score. *arXiv preprint arXiv:2412.15832*.

Larsson, E., Oskarsson, J., Landelius, T., & Lindsten, F. (2025). CRPS-LAM: Regional ensemble weather forecasting from matching marginals. *arXiv preprint arXiv:2510.09484*.

Li, Z., Kovachki, N., Azizzadenesheli, K., Liu, B., Bhattacharya, K., Stuart, A., & Anandkumar, A. (2020). Fourier neural operator for parametric partial differential equations. In *International conference on learning representations*.

Lino, M., Fotiadis, S., Bharath, A. A., & Cantwell, C. (2022). Towards fast simulation of environmental fluid mechanics with multi-scale graph neural networks. In *ICLR 2022 Workshop on AI for Earth and Space Science*.

Lippe, P., Veeling, B., Perdikaris, P., Turner, R., & Brandstetter, J. (2023). PDE-refiner: Achieving accurate long rollouts with neural PDE solvers. In *Advances in neural information processing systems*.

Loshchilov, I., & Hutter, F. (2019). Decoupled weight decay regularization. In *International conference on learning representations*.

Luo, H., Wu, H., Zhou, H., Xing, L., Di, Y., Wang, J., & Long, M. (2025). Transolver++: An accurate neural solver for PDEs on million-scale geometries. In *International conference on machine learning*.

Maharana, A., Cramer, W. D., Samara, E., Scolini, C., Raeder, J., & Poedts, S. (2024). Employing the coupled EUHFORIA-OpenGGCM model to predict CME geoeffectiveness. *Space Weather*, 22(5), e2023SW003715.

Mansouri, R., Kempton, D., Riley, P., & Angryk, R. (2025). Toward data-driven surrogates of the solar wind with spherical Fourier neural operator. *arXiv preprint arXiv:2511.22112*.

Mayank, P., Camporeale, E., Shrivastav, A. K., Berger, T. E., & Arge, C. N. (2025). Neural enhancement of the traditional Wang–Sheeley–Arge solar wind relation. *The Astrophysical Journal Letters*, 994(1), L5.

Mays, M., Taktakishvili, A., Pulkkinen, A., MacNeice, P., Rastätter, L., Odstrcil, D., ... others (2015). Ensemble modeling of CMEs using the WSA–ENLIL+Cone model. *Solar Physics*, 290(6), 1775–1814.

McCabe, M., Mukhopadhyay, P., Marwah, T., Régaldo-Saint Blancard, B., Rozet, F., Diaconu, C., ... Ho, S. (2025). Walrus: A cross-domain foundation model for continuum dynamics. *arXiv preprint arXiv:2511.15684*.

Miles, A., Kirkham, J., Papadopoulos Orfanos, D., Hamman, J., Bussonnier, M., Moore, J., ... Chaudhary, S. (2024). *zarr-developers/zarr-python: v2.18.4*. Zenodo. doi: 10.5281/zenodo.14419265

Mlinarević, M., Holt, G. K., & Agnello, A. (2025). Particle-based plasma simulation using a graph neural network. *arXiv preprint arXiv:2503.00274*.

Molinaro, R., Lanthaler, S., Raonić, B., Rohner, T., Armegioiu, V., Simonis, S., ... Zepeda-Núñez, L. (2025). Generative AI for fast and accurate statistical computation of fluids. *arXiv preprint arXiv:2409.18359*.

Morley, S. K., Welling, D. T., & Woodroffe, J. R. (2018). Perturbed input ensemble modeling with the space weather modeling framework. *Space Weather*, 16(9), 1330–1347.

Mousavi, S., Wen, S., Lingsch, L., Herde, M., Raonić, B., & Mishra, S. (2025). RIGNO: A graph-based framework for robust and accurate operator learning for PDEs on arbitrary domains. In *Advances in neural information processing systems*.

Murray, S. A. (2018). The importance of ensemble techniques for operational space weather forecasting. *Space Weather*, 16(7), 777–783.

Nguyen, T., Koneru, A., Li, S., & Grover, A. (2025). PhysiX: A foundation model for physics simulations. *arXiv preprint arXiv:2506.17774*.

Ohana, R., McCabe, M., Meyer, L., Morel, R., Agocs, F., Beneitez, M., ... others (2024). The Well: A large-scale collection of diverse physics simulations for machine learning. In *Advances in neural information processing systems*.

Oskarsson, J., Landelius, T., Deisenroth, M. P., & Lindsten, F. (2024). Probabilistic weather forecasting with hierarchical graph neural networks. In *Advances in neural information processing systems*.

Pacchiardi, L., Adewoyin, R. A., Dueben, P., & Dutta, R. (2024). Probabilistic forecasting with generative networks via scoring rule minimization. *Journal of Machine Learning Research*, 25(45), 1–64.

Paischer, F., Galletti, G., Hornsby, W., Setinek, P., Zanisi, L., Carey, N., ... Brand-

stetter, J. (2025). GyroSwin: 5D surrogates for gyrokinetic plasma turbulence simulations. In *Advances in neural information processing systems*.

Palmroth, M., Ganse, U., Pfau-Kempf, Y., Battarbee, M., Alho, M., Nättilä, J., ... von Alfthan, S. (2025). Vlasov methods in space physics and astrophysics. *Living Reviews in Computational Astrophysics*, 11(1), 3.

Palmroth, M., Ganse, U., Pfau-Kempf, Y., Battarbee, M., Turc, L., Brito, T., ... von Alfthan, S. (2018). Vlasov methods in space physics and astrophysics. *Living Reviews in Computational Astrophysics*, 4(1), 1.

Palmroth, M., Hoilijoki, S., Juusola, L., Pulkkinen, T. I., Hietala, H., Pfau-Kempf, Y., ... Hesse, M. (2017). Tail reconnection in the global magnetospheric context: Vlasiator first results. In *Annales geophysicae* (Vol. 35, pp. 1269–1274).

Palmroth, M., Pulkkinen, T. I., Ganse, U., Pfau-Kempf, Y., Koskela, T., Zaitsev, I., ... others (2023). Magnetotail plasma eruptions driven by magnetic reconnection and kinetic instabilities. *Nature Geoscience*, 16(7), 570–576.

Papadakis, K., Alho, M., Kataja, J., Bouri, I., Kit, A., Heikonen, J., & Palmroth, M. (2025). Neural networks as a lossy compression and restart/recovery strategy for high-dimensional plasma simulations. *Physics of Plasmas*, 32(11).

Parker, L., Lanusse, F., Shen, J., Liu, O., Hehir, T., Sarra, L., ... Ho, S. (2025). AION-1: Omnimodal foundation model for astronomical sciences. In *Neural information processing systems*.

Pedersen, C., Zanna, L., & Bruna, J. (2025). Thermalizer: Stable autoregressive neural emulation of spatiotemporal chaos. In *International conference on machine learning*.

Pfaff, T., Fortunato, M., Sanchez-Gonzalez, A., & Battaglia, P. W. (2021). Learning mesh-based simulation with graph networks. In *International conference on learning representations*.

Pfau-Kempf, Y., Ganse, U., Battarbee, M., Kotipalo, L., Koskela, T., von Alfthan, S., ... Horaites, K. (2024). *fmihpc/vlasiator: v5.3.1*. Zenodo. doi: 10.5281/zenodo.13752779

Price, I., Sanchez-Gonzalez, A., Alet, F., Andersson, T. R., El-Kadi, A., Masters, D., ... others (2025). Probabilistic weather forecasting with machine learning. *Nature*, 637(8044), 84–90.

Rasp, S., & Lerch, S. (2018). Neural networks for postprocessing ensemble weather forecasts. *Monthly Weather Review*, 146(11), 3885–3900.

Roy, S., Schmude, J., Lal, R., Gaur, V., Freitag, M., Kuehnert, J., ... others (2025). Surya: Foundation model for heliophysics. *arXiv preprint arXiv:2508.14112*.

Sanchez-Gonzalez, A., Godwin, J., Pfaff, T., Ying, R., Leskovec, J., & Battaglia, P. (2020). Learning to simulate complex physics with graph networks. In *International conference on machine learning*.

Sohn, K., Lee, H., & Yan, X. (2015). Learning structured output representation using deep conditional generative models. In *Advances in neural information processing systems*.

Stone, E. C., Frandsen, A., Mewaldt, R., Christian, E., Margolies, D., Ormes, J., & Snow, F. (1998). The advanced composition explorer. *Space Science Reviews*, 86(1), 1–22.

Suni, J., Palmroth, M., Turc, L., Battarbee, M., Pfau-Kempf, Y., & Ganse, U. (2025). Magnetosheath jets associated with a solar wind rotational discontinuity in a hybrid-Vlasov simulation. *Journal of Geophysical Research: Space Physics*, 130(6), e2025JA033995.

Tali, R., Rabeh, A., Yang, C.-H., Shadkhah, M., Karki, S., Upadhyaya, A., ... others (2024). Flowbench: A large scale benchmark for flow simulation over complex geometries. *arXiv preprint arXiv:2409.18032*.

Turc, L., Roberts, O. W., Verscharen, D., Dimmock, A. P., Kajdič, P., Palmroth, M., ... others (2023). Transmission of foreshock waves through Earth's bow shock. *Nature Physics*, 19(1), 78–86.

Turner, H., Lang, M., Owens, M., Smith, A., Riley, P., Marsh, M., & Gonzi, S. (2023). Solar wind data assimilation in an operational context: Use of near-real-time data and the forecast value of an L5 monitor. *Space Weather*, 21(5), e2023SW003457.

Utkarsh, U., Cai, P., Edelman, A., Gomez-Bombarelli, R., & Rackauckas, C. V. (2025). Physics-constrained flow matching: Sampling generative models with hard constraints. In *Neural information processing systems*.

Valencia, M. L., Pfaff, T., & Thuerey, N. (2025). Learning distributions of complex fluid simulations with diffusion graph networks. In *International conference on learning representations*.

Vigot, G., Cuenot, B., Vermorel, O., & Bauerheim, M. (2025). Graph neural networks for computational plasma physics on unstructured grids: Application to approximate the poisson equation for Hall-Effect thrusters modeling. *Journal of Electric Propulsion*, 4(1), 46.

Von Alfthan, S., Pokhotelov, D., Kempf, Y., Hoilijoki, S., Honkonen, I., Sandroos, A., & Palmroth, M. (2014). Vlasiator: First global hybrid-Vlasov simulations of Earth's foreshock and magnetosheath. *Journal of Atmospheric and Solar-Terrestrial Physics*, 120, 24–35.

Zaitsev, I., Holmberg, D., Alho, M., Bouri, I., Franssila, F., Jeong, H., … Roos, T. (2025). *Vlasiator dataset for machine learning studies*. Hugging Face. doi: 10.57967/hf/7027

Zamo, M., & Naveau, P. (2018). Estimation of the continuous ranked probability score with limited information and applications to ensemble weather forecasts. *Mathematical Geosciences*, 50(2), 209–234.

Zhang, Y., Paxton, L. J., Schaefer, R., & Swartz, W. H. (2022). Thermospheric conditions associated with the loss of 40 Starlink satellites. *Space Weather*, 20(10), e2022SW003168.

Supporting Information for

Deterministic and Probabilistic Neural Surrogates of Global Hybrid-Vlasov Simulations

Daniel Holmberg^{1,3}, Ivan Zaitsev², Markku Alho², Ioanna Bouri¹, Fanni Franssila¹, Haewon Jeong³, Minna Palmroth^{2,4}, and Teemu Roos¹

¹Department of Computer Science, University of Helsinki

²Department of Physics, University of Helsinki

³Department of Electrical and Computer Engineering, University of California, Santa Barbara

⁴Space and Earth Observation Centre, Finnish Meteorological Institute

Contents of this file

Figures S1 to S12

Introduction

This supplement provides additional results and visualizations. We include example forecasts for the in-plane components of the electromagnetic and velocity fields, together with the out-of-plane electric field component E_y shown in Figure S4, which is of particular interest in this configuration because it is oriented along the direction where magnetic reconnection occurs. For example, in Run 4 there is a visible flux transfer event at the subsolar magnetopause, where Graph-EFM produces a strong reconnection electric field. We also provide forecast evaluation metrics, including RMSE, CRPS, and SSR, for all variables not shown in the main text. Similarly, the spatial power spectra for all remaining variables are included here that compare deterministic and probabilistic forecasts with the Vlasiator simulator. Finally, density plots comparing predicted values with the simulator are shown for lead times of 10 s and 50 s, to give a better idea how these change over time.

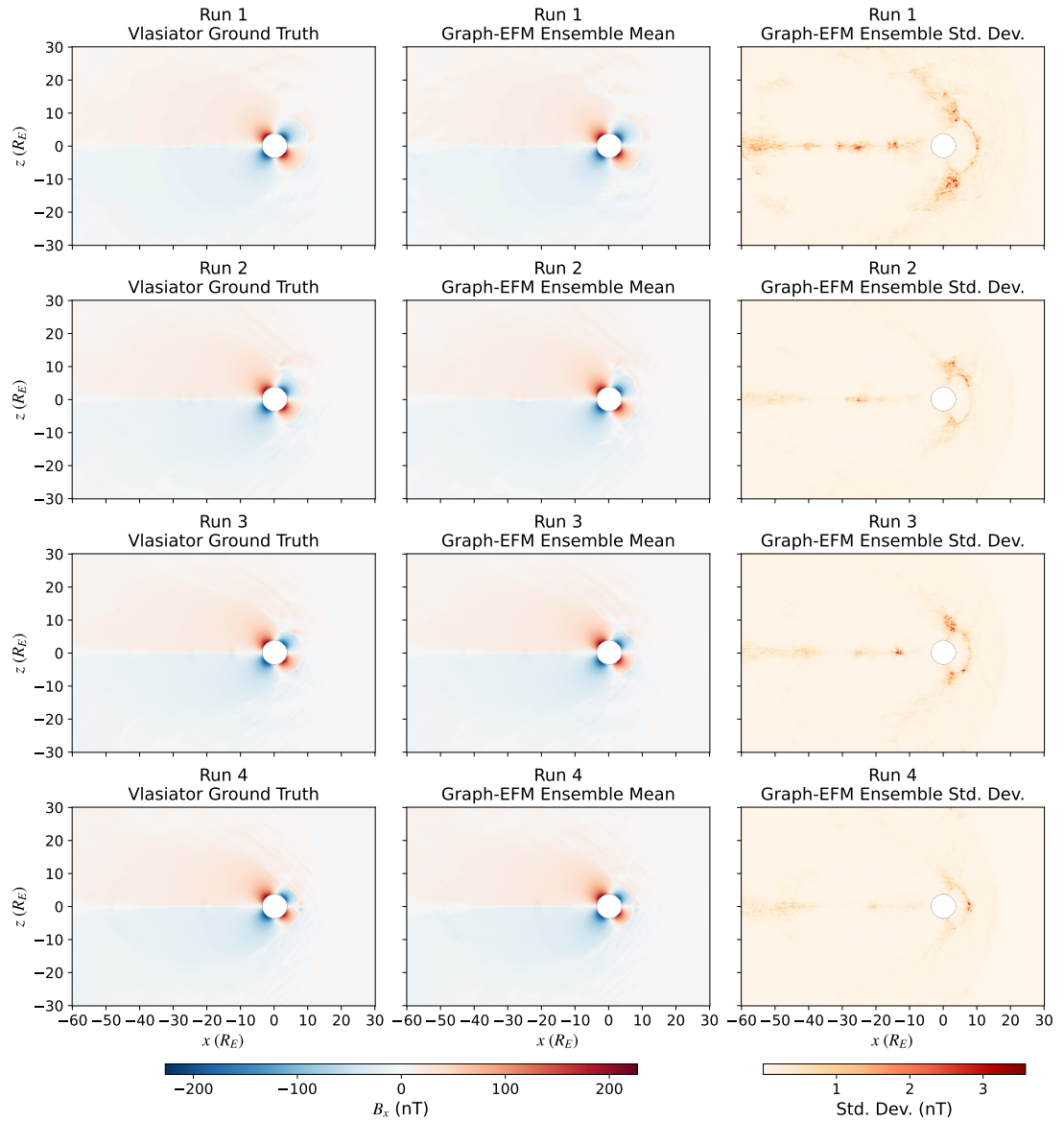


Figure S1: Example B_x Vlasiorator ground truth, Graph-EFM ensemble mean, and forecast uncertainty for each run at lead time $t = 30$ s for a forecast in the test set.

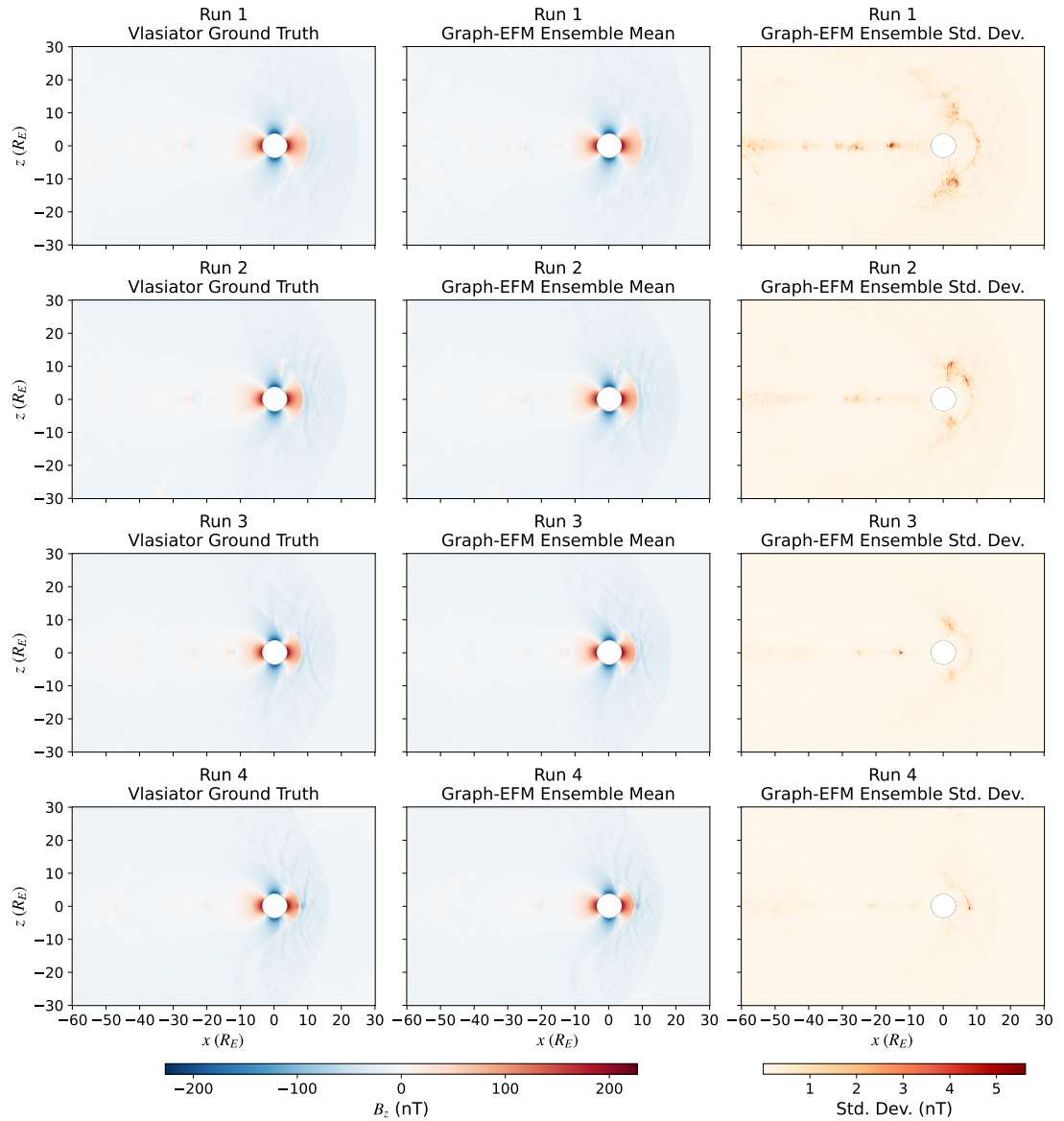


Figure S2: Example B_z Vlasiorator ground truth, Graph-EFM ensemble mean, and forecast uncertainty for each run at lead time $t = 30$ s for a forecast in the test set.

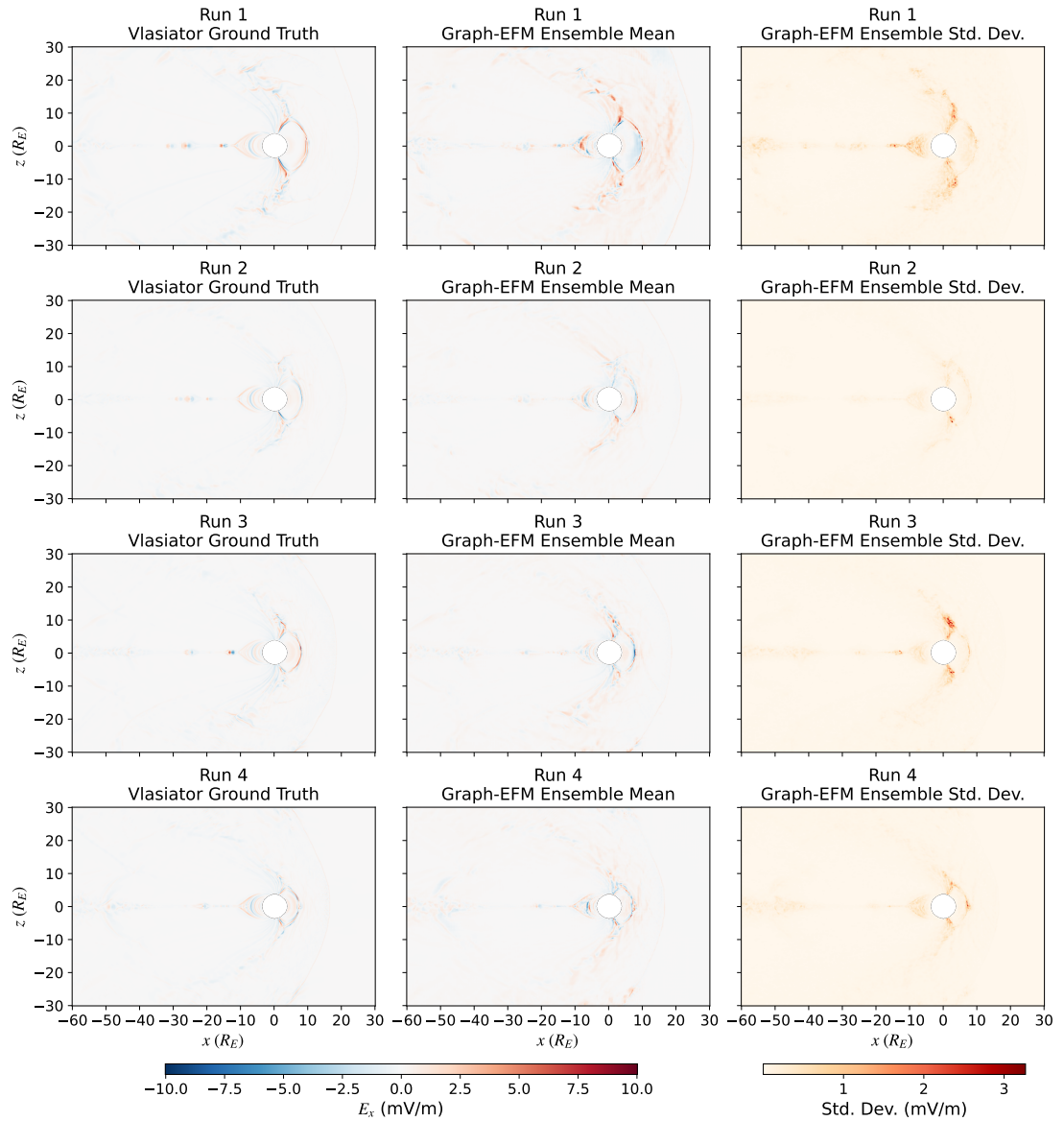


Figure S3: Example E_x Vlasiorator ground truth, Graph-EFM ensemble mean, and forecast uncertainty for each run at lead time $t = 30$ s for a forecast in the test set.

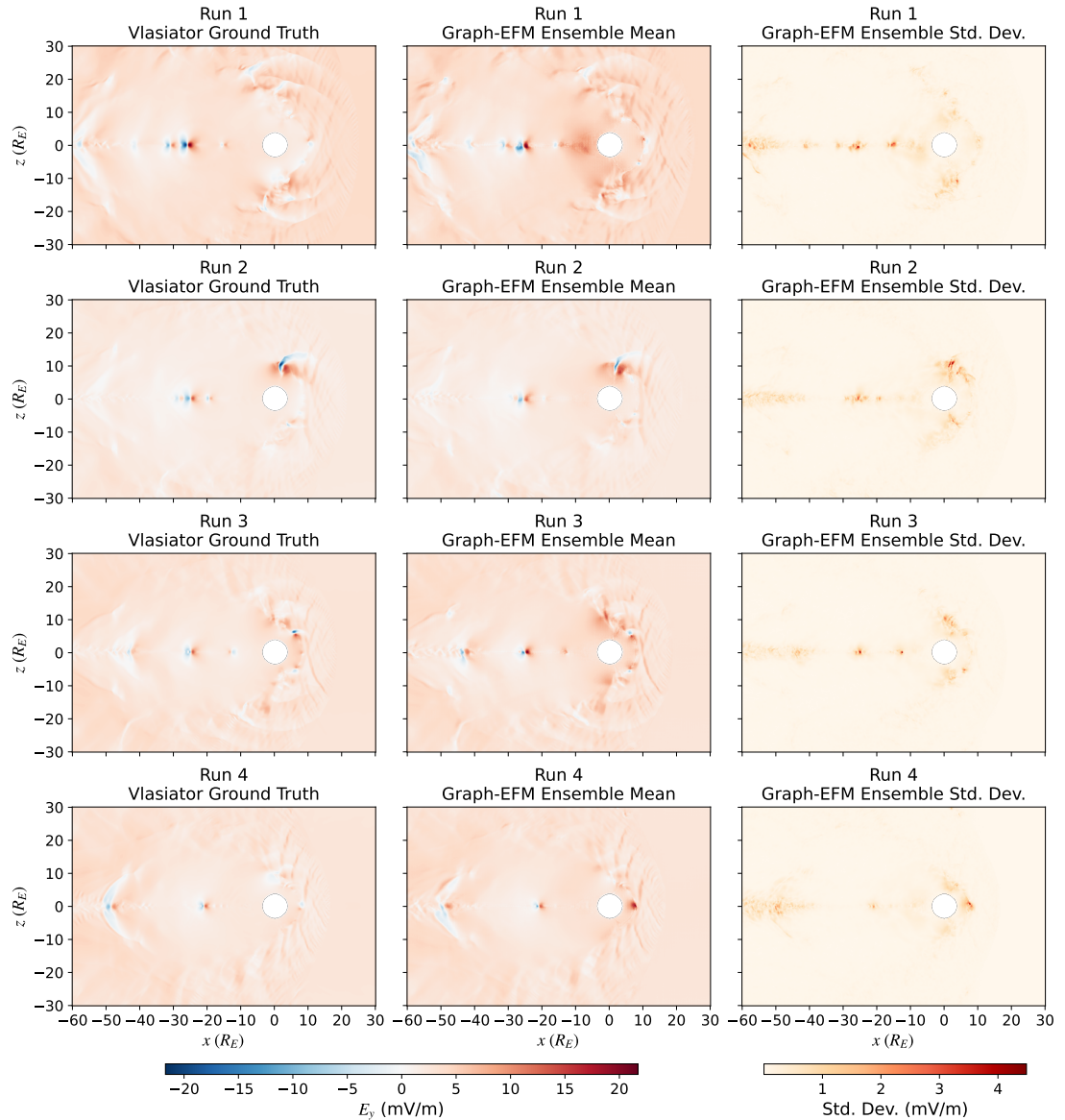


Figure S4: Example E_y Vlasiorator ground truth, Graph-EFM ensemble mean, and forecast uncertainty for each run at lead time $t = 30$ s for a forecast in the test set.

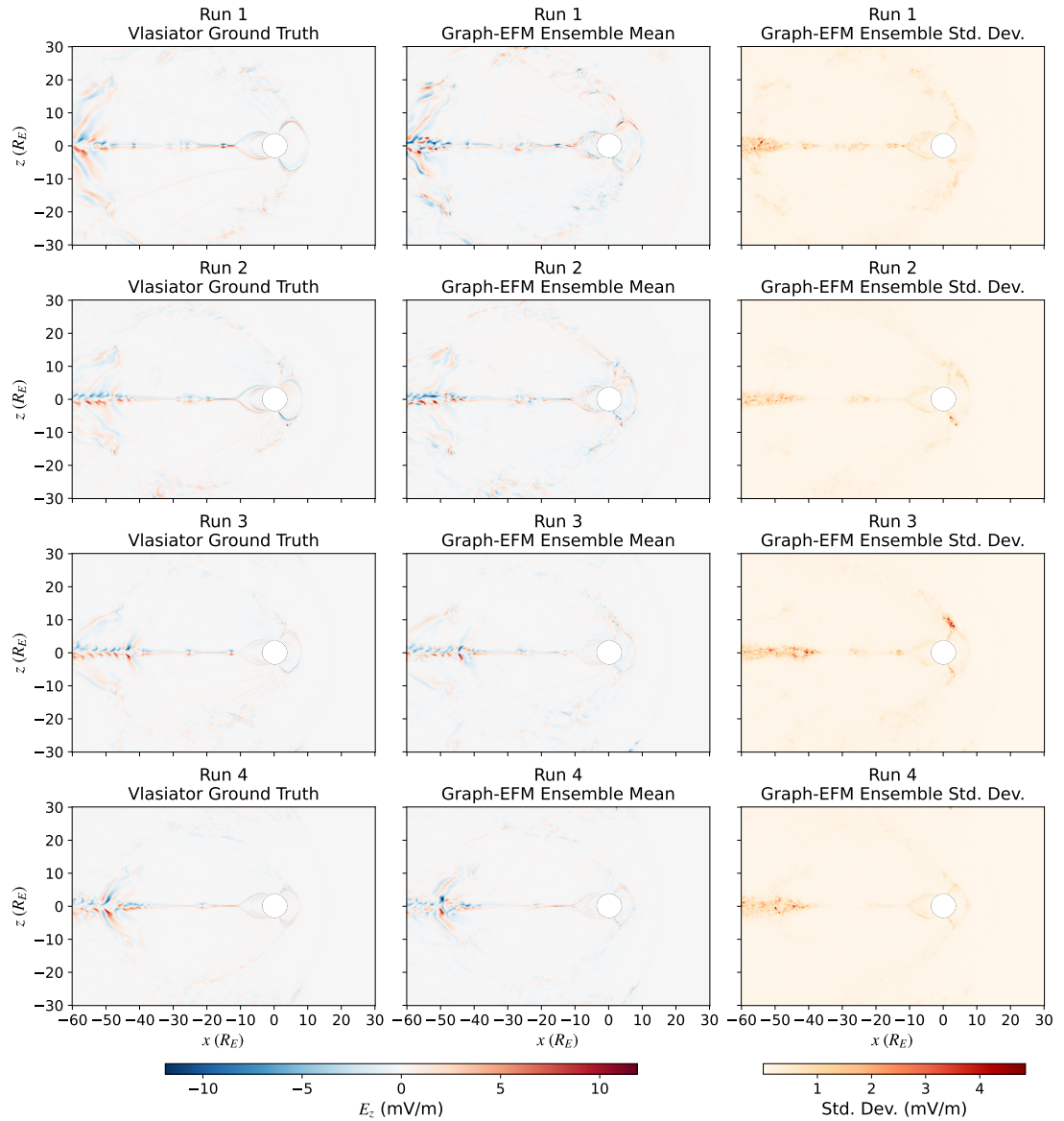


Figure S5: Example E_z Vlasiorator ground truth, Graph-EFM ensemble mean, and forecast uncertainty for each run at lead time $t = 30$ s for a forecast in the test set.

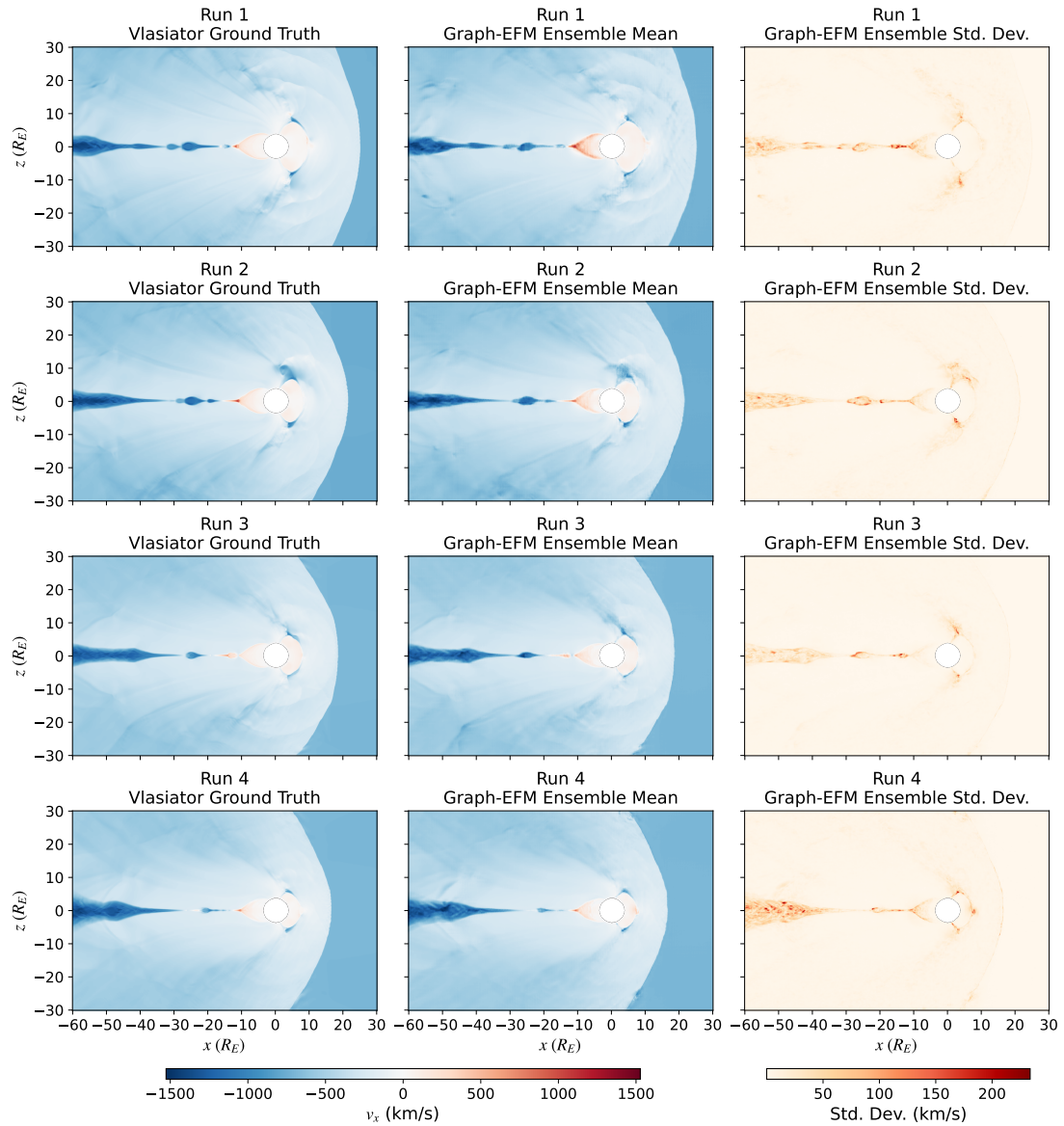


Figure S6: Example v_x Vlasiorator ground truth, Graph-EFM ensemble mean, and forecast uncertainty for each run at lead time $t = 30$ s for a forecast in the test set.

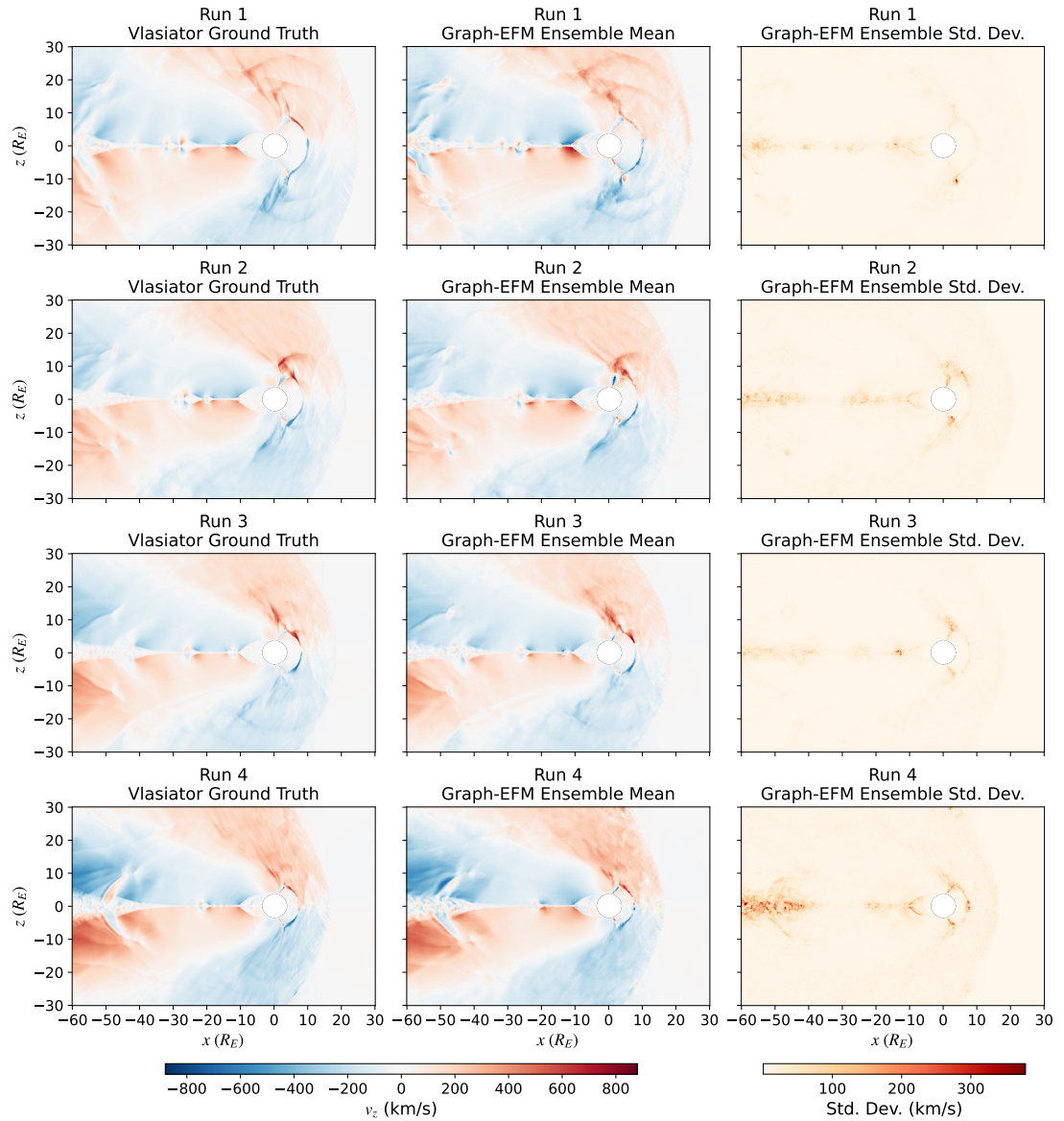


Figure S7: Example v_z Vlasiorator ground truth, Graph-EFM ensemble mean, and forecast uncertainty for each run at lead time $t = 30$ s for a forecast in the test set.

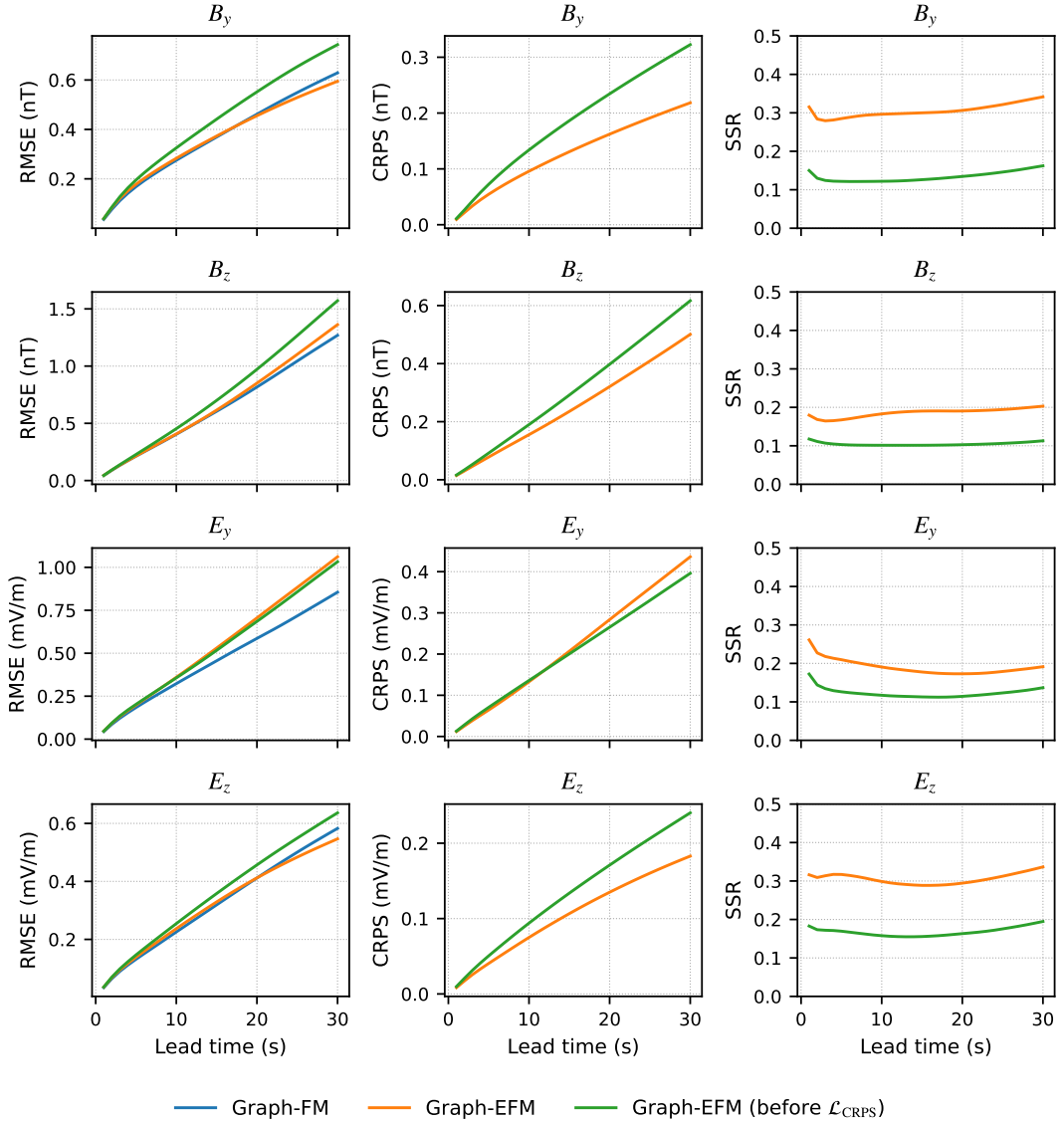


Figure S8: Forecast performance on the test set indicated by RMSE, CRPS, and SSR for all deterministic (Graph-FM) and probabilistic (Graph-EFM) models across variables B_y , B_z , E_y , and E_z for lead times 1–30 s.

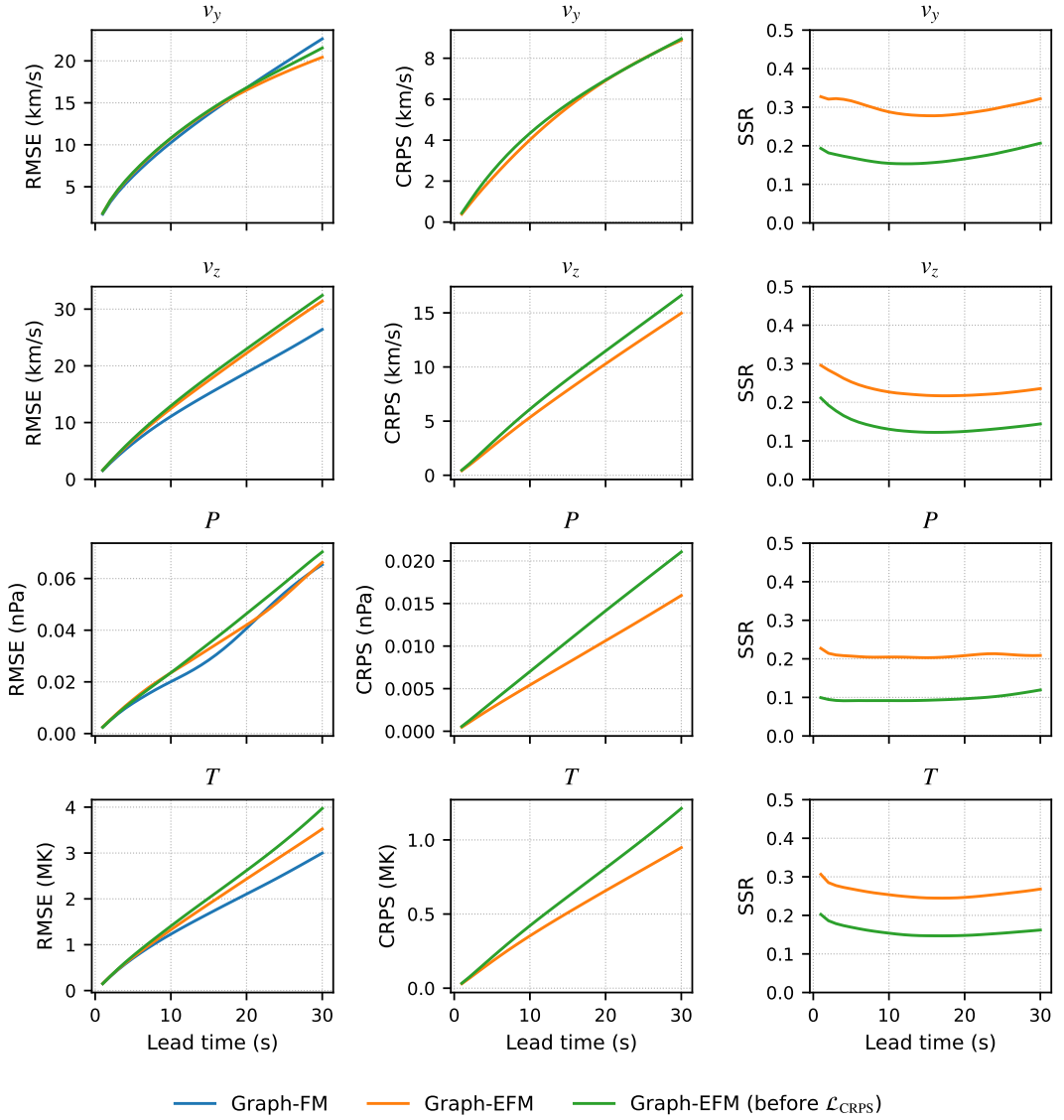


Figure S9: Forecast performance on the test set indicated by RMSE, CRPS, and SSR for all deterministic (Graph-FM) and probabilistic (Graph-EFM) models across variables v_y , v_z , P , and T for lead times 1–30 s.

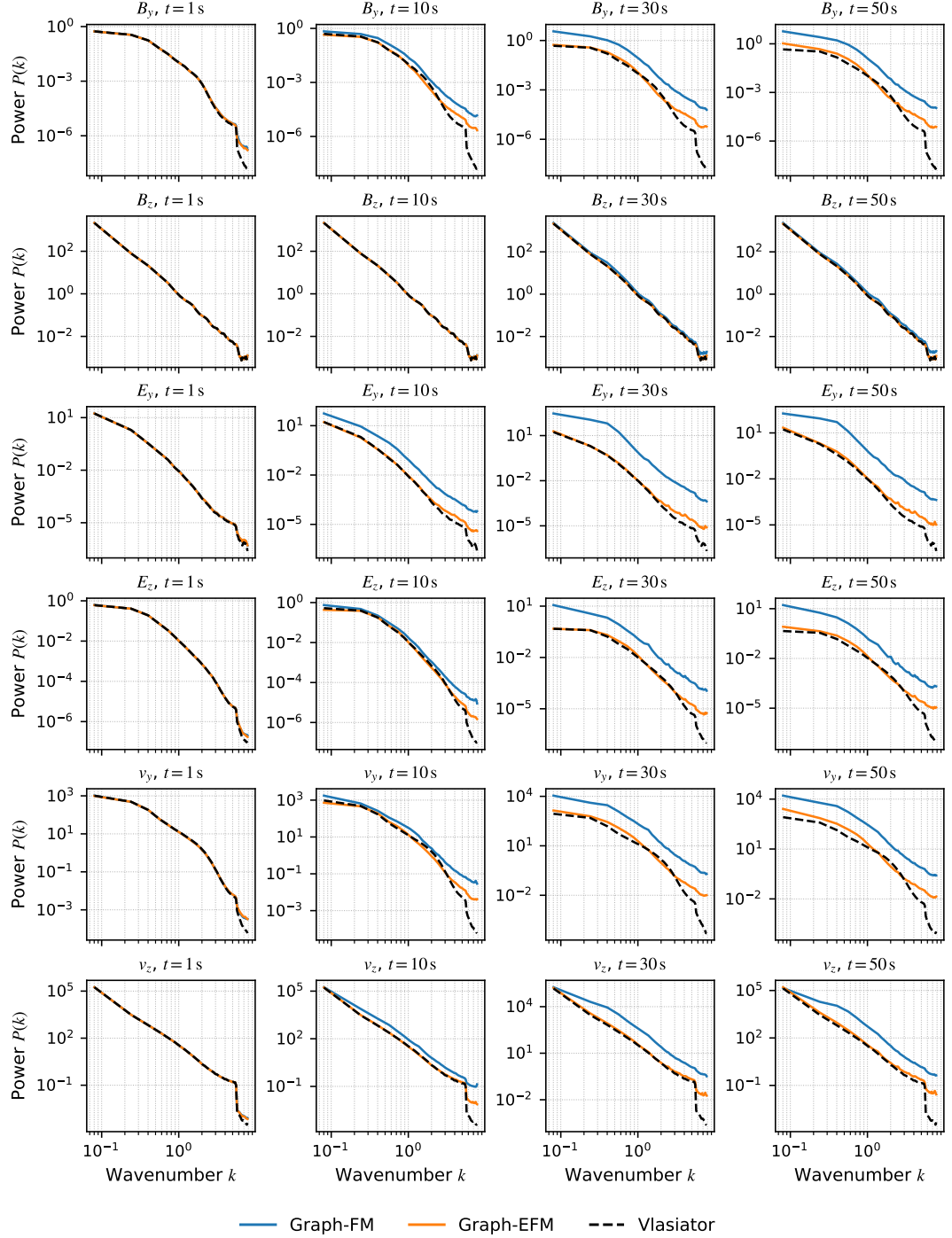


Figure S10: Spatial power spectra of B_y , B_z , E_y , E_z , v_y and v_z . Each panel shows the isotropic power $P(k)$ versus wavenumber k , comparing Graph-FM and Graph-EFM forecasts with the Vlasiator ground truth at forecast lead times of $t = 1, 10, 30$, and 50 s.

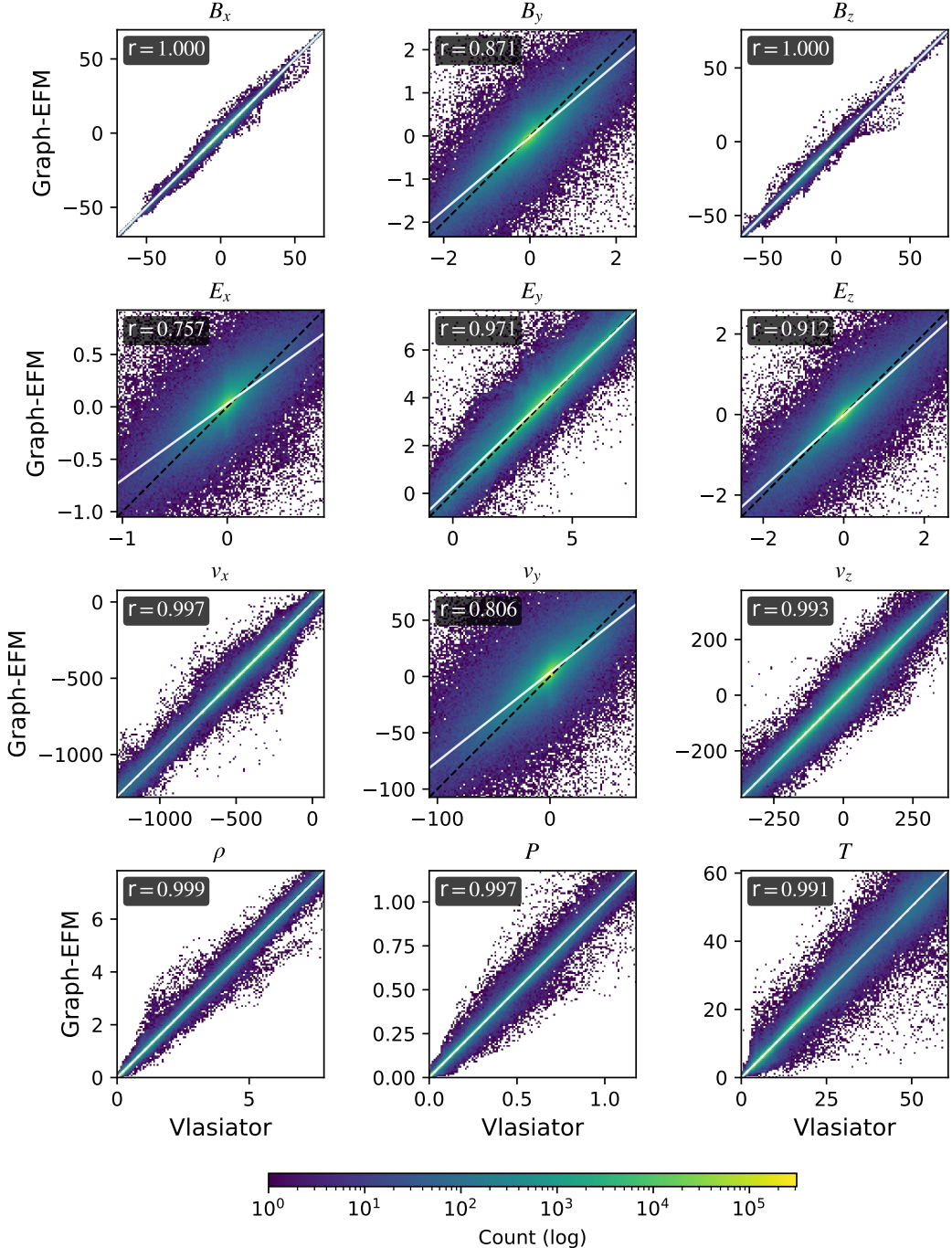


Figure S11: Two-dimensional density plots illustrating the relationship between predicted and ground truth for Graph-EFM at a lead time of $t = 10$ s are shown for each physical variable. Each panel aggregates results from four forecasts. Colors represent logarithmic point density, the dotted line indicates the one-to-one relation, the solid line shows the least-squares fit, and the annotated Pearson coefficient summarizes linear correlation.

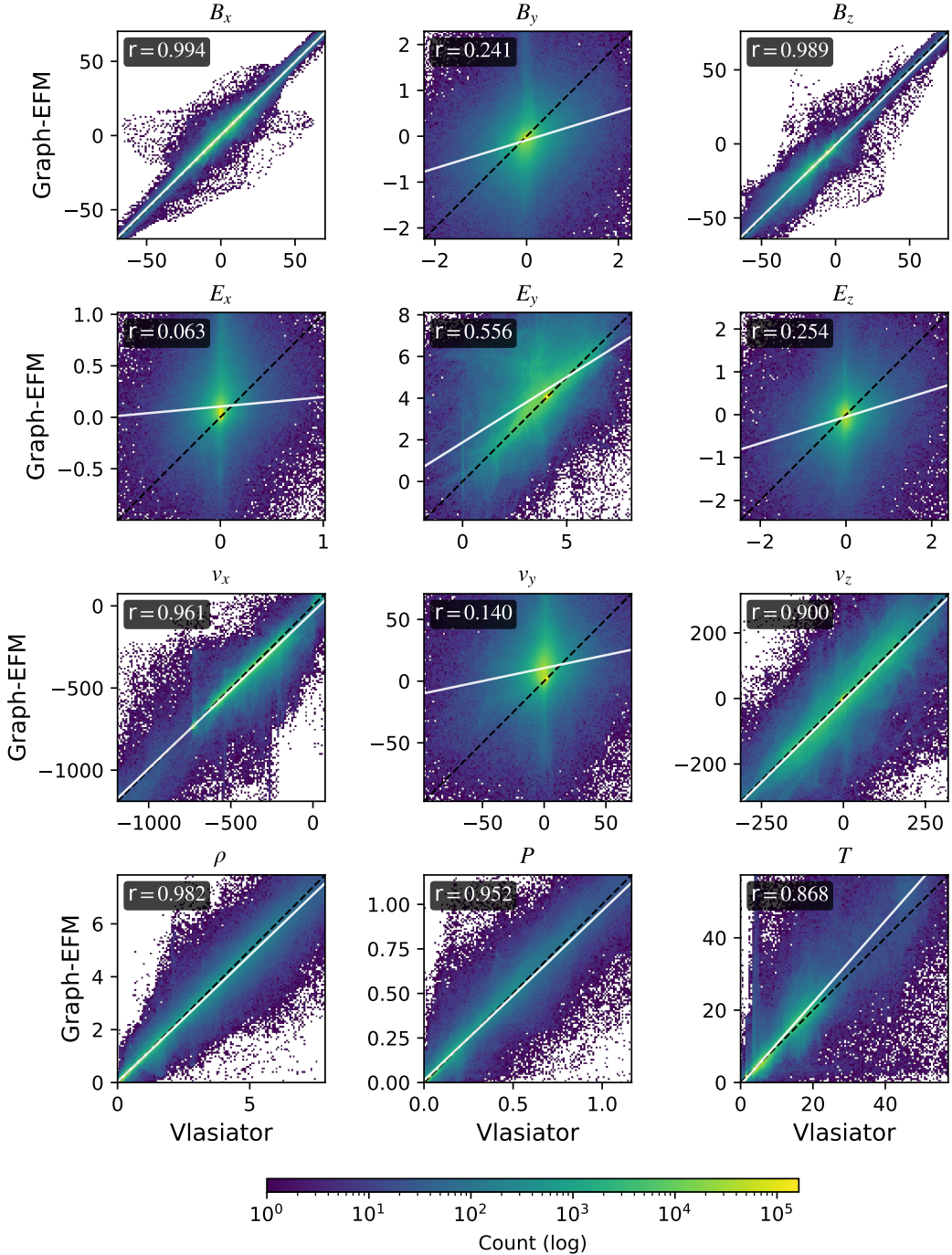


Figure S12: Two-dimensional density plots illustrating the relationship between predicted and ground truth for Graph-EFM at a lead time of $t = 50$ s are shown for each physical variable. Each panel aggregates results from four forecasts. Colors represent logarithmic point density, the dotted line indicates the one-to-one relation, the solid line shows the least-squares fit, and the annotated Pearson coefficient summarizes linear correlation.